Open Source Combustion Instability Low Order Simulator (OSCILOS–Long)
Technical report

Jingxuan Li, Dong Yang, Charles Luzzato and Aimee S. Morgans [1]
Department of Aeronautics, Imperial College London, UK

1 Introduction

Combustion instability has been a major issue in the design of industrial gas turbines and aeroengines for several decades. It arises due to the coupling between the unstable combustion process and acoustic disturbances within the combustion chamber. The mechanism can be briefly described as: acoustic noise with a broad frequency bandwidth is produced during the combustion process [1]. These sound waves propagate inside the combustion chamber, interact with the boundaries and return back to the combustion zone with a time delay that depends on the size of the combustion chamber, disturbances of speed of sound and impedances at the boundaries of the combustion chamber. These pressure oscillations generate in turn perturbations of the flow field by modifying the local flowrate, reactant composition or thermodynamic properties in the flame region, producing heat release rate disturbances [2, 3]. When these disturbances are synchronised, they amplify leading to an increase of acoustic energy in the system and a resonance is generally observed at specific tones. These self-sustained instabilities are more likely to happen in lean premixed combustion systems, which offer the potential for reducing NO_x emissions in modern gas turbine design [4].

Combustion instabilities are generally not desirable because they may lead to an early ageing of the combustion chamber or even to severe structural damage [5]. Knowledge of this complex mechanism is necessary in the development of control strategies. The open source combustion instability low-order simulator (OSCILOS) is an open source code for simulating combustion instability. It is written in Matlab® / Simulink® and is very straightforward to run and edit. It can simulate both longitudinal and annular combustor geometries. It represents a combustor as a network of connected modules. The acoustic waves are modeled as either 1-D plane waves (longitudinal combustors) or 2-D plane/circumferential waves (annular combustors). A variety of inlet and exit

---

[1]Corresponding author: *a.morgans@imperial.ac.uk*
More details and code downloads can be found at `www.oscilos.com`. The latest version of OSCILOS is also available from our Github repository: `https://github.com/MorgansLab/`. Contributions are welcome and can be submitted with GitHub pull request. These will be reviewed and accepted by the team.

acoustic boundary conditions are possible, including open, closed, choked and user defined boundary conditions. The response of the flame to acoustic waves is captured via a flame model; flame models ranging from linear $n - \tau$ models to non-linear flame describing functions, either prescribed analytically or loaded from experiment / CFD data, can be prescribed. The mean flow is calculated simply by assuming 1-D flow conditions, with changes only across module interfaces or flames. This current version is for longitudinal modes. This assumes a longitudinal/cannular/can combustor geometry, or an annular geometry but where only plane acoustic waves are known to be of interest.

2 Acoustic wave equations

Analysis is carried out on a model combustion chamber which is schematically described in Figure 1. The configuration consists of several cylindrical tubes with different sectional areas. Denoting the distance along the longitudinal axis by the vector x, the inlet and outlet of section k are at $x = x_{k-1}$ and $x = x_k$ respectively, where $k = 1, 2, \ldots N$. A premixed gaseous flame located at $x = x_n$ (n is integer and $0 \leq n \leq N$) is used as the heat source. The fully mixed fresh gases are ignited and rapidly turn to burned gases.

In the analysis, the following assumptions are implemented:

- The envisaged frequencies are assumed sufficiently small to consider the combustion zone to be "compact" [2] compared to the acoustic wavelength and to only take into account the longitudinal waves. The acoustic field can thus be described by the superposition of forward and backward propagating plane waves.

- The fluids before and after the combustion zone are assumed to be perfect gases. The temperature T can be expressed as a function of pressure p and density ρ.

- Entropy waves are mainly formed during the unsteady combustion process. Vorticity is neglected in the current analysis.

Now consider weak disturbances induced inside the combustor. Acoustic waves propagate in both directions. The pressure, velocity and density in section k can be expressed as:

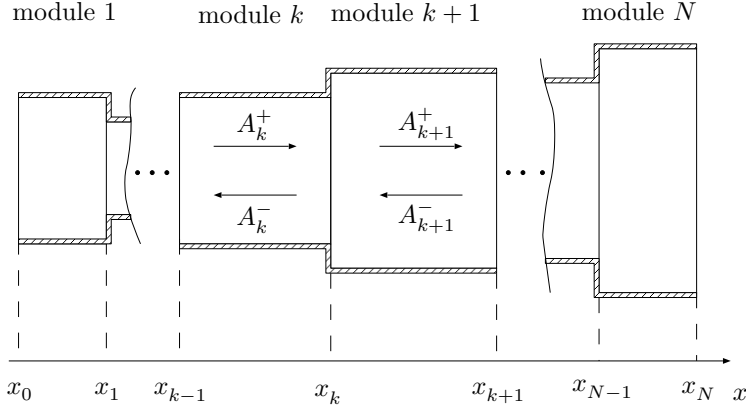[2]although it is possible to implement several staged combustion zones.

Figure 1: Schematic view of the long sectional area change combustor.

$$p_k(x, t) = \bar{p}_k + p'_k(x, t) = \bar{p}_k + A_k^+\left(t - \tau_k^+\right) + A_k^-\left(t - \tau_k^-\right) \tag{1a}$$

$$u_k(x, t) = \bar{u}_k + u'_k(x, t) = \bar{u}_k + \frac{1}{\bar{\rho}_k \bar{c}_k}\left[A_k^+\left(t - \tau_k^+\right) - A_k^-\left(t - \tau_k^-\right)\right] \tag{1b}$$

$$\rho_k(x, t) = \bar{\rho}_k + \rho'_k(x, t) = \bar{\rho}_k + \frac{1}{\bar{c}_k^2}\left[A_k^+\left(t - \tau_k^+\right) + A_k^-\left(t - \tau_k^-\right)\right] - \frac{1}{\bar{c}_k^2}E_k\left(t - \tau_k^s\right) \tag{1c}$$

where A_k^+ and A_k^- denote the amplitude of the downstream and upstream propagating acoustic waves respectively. $E_k = \bar{\rho}_k \bar{c}_k^2 / C_{p,k} s'_k$ represents the amplitude of entropy waves. $\tau_k^+ = (x - x_{k-1})\big/(\bar{c}_k + \bar{u}_k)$, $\tau_k^- = (x_k - x)\big/(\bar{c}_k - \bar{u}_k)$ and $\tau_k^s = (x - x_{k-1})/\bar{u}_k$ are time delays.

3

2.1 Without heat addition

2.1.1 Area increase

It is necessary to link the thermal properties and mean flow variables between neighbouring combustor sections. We firstly consider the case without heat addition. At the area increase interface, the mass and energy flux are unchanged, however the momentum flux is increased by the axial force on the walls [6]. We thus have the relations:

$$\Theta_k \rho_{k+1}(x_k, t)u_{k+1}(x_k, t) = \rho_k(x_k, t)u_k(x_k, t) \tag{2a}$$

$$p_{k+1}(x_k, t) + \rho_{k+1}(x_k, t)u_{k+1}^2(x_k, t) = p_k(x_k, t) + \frac{1}{\Theta_k}\rho_k(x_k, t)u_k^2(x_k, t) \tag{2b}$$

$$H_{k+1}(x_k, t) = H_k(x_k, t) \tag{2c}$$

where H is the enthalpy of the flux and $\Theta_k = S_{k+1}/S_k$ denotes the ratio of sectional surface areas. Considering weak disturbances, the high order terms can be neglected and it is possible to write out the stationary and first order term forms to relate the upstream and downstream acoustic waves. The stationary forms of the conservation equations give:

$$\Theta_k \bar{\rho}_{k+1}\bar{u}_{k+1} = \bar{\rho}_k\bar{u}_k \tag{3a}$$

$$\bar{p}_{k+1} + \bar{\rho}_{k+1}\bar{u}_{k+1}^2 = \bar{p}_k + \frac{1}{\Theta_k}\bar{\rho}_k\bar{u}_k^2 \tag{3b}$$

$$\frac{\gamma}{\gamma - 1}\left(\Theta_k\bar{p}_{k+1}\bar{u}_{k+1} - \bar{p}_k\bar{u}_k\right) + \frac{1}{2}\bar{\rho}_k\bar{u}_k\left(\bar{u}_{k+1}^2 - \bar{u}_k^2\right) = 0 \tag{3c}$$

The first order forms in the Laplace domain give:

$$\mathcal{B}_{k,2}\begin{bmatrix} \tilde{p}_{k+1}(x_k, s) \\ \bar{\rho}_{k+1}\bar{c}_{k+1}\tilde{u}_{k+1}(x_k, s) \\ \tilde{\rho}_{k+1}(x_k, s)\bar{c}_{k+1}^2 \end{bmatrix} = \mathcal{B}_{k,1}\begin{bmatrix} \tilde{p}_k(x_k, s) \\ \bar{\rho}_k\bar{c}_k\tilde{u}_k(x_k, s) \\ \tilde{\rho}_k(x_k, s)\bar{c}_k^2 \end{bmatrix} \tag{4}$$

4

where,

$$
\mathcal{B}_{k,1} =
\begin{bmatrix}
0 & \dfrac{\bar{c}_{k+1}}{\bar{c}_k} & \bar{M}_k \dfrac{\bar{c}_{k+1}}{\bar{c}_k} \\[2ex]
\Theta_k & 2\bar{M}_k & \bar{M}_k^2 \\[2ex]
\dfrac{\gamma}{\gamma-1}\bar{M}_k & \bar{M}_k^2 & -\dfrac{1}{\gamma-1}\bar{M}_k
\end{bmatrix}
\tag{5a}
$$

$$
\mathcal{B}_{k,2} = \Theta_k
\begin{bmatrix}
0 & 1 & \bar{M}_{k+1} \\[2ex]
1 & 2\bar{M}_{k+1} & \bar{M}_{k+1}^2 \\[2ex]
\dfrac{\gamma}{\gamma-1}\dfrac{\bar{c}_{k+1}}{\bar{c}_k}\bar{M}_{k+1} & \dfrac{\bar{c}_{k+1}}{\bar{c}_k}\bar{M}_{k+1}^2 & -\dfrac{1}{\gamma-1}\dfrac{\bar{c}_{k+1}}{\bar{c}_k}\bar{M}_{k+1}
\end{bmatrix}
\tag{5b}
$$

The superscript $\tilde{}$ indicates the Laplace transform. $s = \sigma + i2\pi f$ represents the Laplace variable, σ is the growth rate and f denotes the frequency.

2.1.2 Area decrease

At an area decrease interface, the mass and energy flux are unchanged. The flow through the area change interface can be assumed isentropic. The momentum equation is replaced by:

$$
\frac{p_{k+1}(x_k, t)}{\rho_{k+1}^{\gamma}(x_k, t)} = \frac{p_k(x_k, t)}{\rho_k^{\gamma}(x_k, t)}
\tag{6}
$$

with its stationary forms:

$$
\frac{\bar{p}_{k+1}}{\bar{\rho}_{k+1}^{\gamma}} = \frac{\bar{p}_k}{\bar{\rho}_k^{\gamma}}
\tag{7}
$$

5

and the corresponding coefficients of the first order forms in the Laplace domain:

$$
\mathcal{B}_{k,1} =
\begin{bmatrix}
0 & \dfrac{\bar{c}_{k+1}}{\bar{c}_k} & \bar{M}_k \dfrac{\bar{c}_{k+1}}{\bar{c}_k} \\[3mm]
\dfrac{1}{\bar{\rho}_k^{\gamma}} & 0 & -\dfrac{1}{\bar{\rho}_k^{\gamma}} \\[3mm]
\dfrac{\gamma}{\gamma-1}\bar{M}_k & \bar{M}_k^2 & -\dfrac{1}{\gamma-1}\bar{M}_k
\end{bmatrix}
\tag{8a}
$$

$$
\mathcal{B}_{k,2} = \Theta_k
\begin{bmatrix}
0 & 1 & \bar{M}_{k+1} \\[3mm]
\dfrac{1}{\Theta_k \bar{\rho}_{k+1}^{\gamma}} & 0 & -\dfrac{1}{\Theta_k \bar{\rho}_{k+1}^{\gamma}} \\[3mm]
\dfrac{\gamma}{\gamma-1}\dfrac{\bar{c}_{k+1}}{\bar{c}_k}\bar{M}_{k+1} & \dfrac{\bar{c}_{k+1}}{\bar{c}_k}\bar{M}_{k+1}^2 & -\dfrac{1}{\gamma-1}\dfrac{\bar{c}_{k+1}}{\bar{c}_k}\bar{M}_{k+1}
\end{bmatrix}
\tag{8b}
$$

2.2 With heat addition

We now consider the case with flame. In general, the flame is located at an area increase interface. We thus can assume that the change of the flow across this interface has two steps: the flow expands at the position of the abrupt area increase and is then heated by the flame. It is thus possible to write out the link of thermal properties and mean flow across the flame.

(i) Expansion:

$$
\Theta_k \rho_{k+\frac{1}{2}}(x_k,t) u_{k+\frac{1}{2}}(x_k,t) = \rho_k(x_k,t) u_k(x_k,t)
\tag{9a}
$$

$$
p_{k+\frac{1}{2}}(x_k,t) + \rho_{k+\frac{1}{2}}(x_k,t) u_{k+\frac{1}{2}}^2(x_k,t) = p_k(x_k,t) + \frac{1}{\Theta_k}\rho_k(x_k,t) u_k^2(x_k,t)
\tag{9b}
$$

$$
H_{k+\frac{1}{2}}(x_k,t) = H_k(x_k,t)
\tag{9c}
$$

(ii) Heat addition:

$$\rho_{k+1}(x_k,t)u_{k+1}(x_k,t) = \rho_{k+\frac{1}{2}}(x_k,t)u_{k+\frac{1}{2}}(x_k,t) \tag{10a}$$

$$p_{k+1}(x_k,t) + \rho_{k+1}(x_k,t)u_{k+1}^2(x_k,t) = p_{k+\frac{1}{2}}(x_k,t) + \rho_{k+\frac{1}{2}}(x_k,t)u_{k+\frac{1}{2}}^2(x_k,t) \tag{10b}$$

$$\rho_{k+1}(x_k,t)u_{k+1}(x_k,t)H_{k+1}(x_k,t) = \rho_{k+\frac{1}{2}}(x_k,t)u_{k+\frac{1}{2}}(x_k,t)H_{k+\frac{1}{2}}(x_k,t) + \dot{q}(t) \tag{10c}$$

$$p_k(x_k,t) = \rho_k(x_k,t)R_{g,1}T_k(x_k,t), \quad p_{k+\frac{1}{2}}(x_k,t) = \rho_{k+\frac{1}{2}}(x_k,t)R_{g,2}T_{k+\frac{1}{2}}(x_k,t) \tag{10d}$$

where $\dot{q}(t)$ denotes the heat release rate per surface area. In general, the temperature ratio across the flame $\bar{T}_{k+1}/\bar{T}_k \approx 5 - 7$ for hydrocarbon flames and the heat capacity C_p depends on temperature and can not be considered constant. The enthalpy of the flow should thus be expressed as

$$\bar{H} = \int_{\bar{T}_0}^{\bar{T}} C_p \mathrm{d}T + \frac{1}{2}\bar{u}_k^2 \tag{11}$$

where $\bar{T}_0 = 298.15$ K. The heat release rate $\dot{q}$ is from the reaction of the fuel or from the heating grid in case of a Rijke tube. Herein, it is important to note that the heat capacity ratio γ varies across the flame. To simplify the calculation, we use γ_1 and γ_2 to represent the heat capacity ratio in the combustor sections before and after the flame. The determination of the temperature of the reactants and γ_2 are detailed in Appendix A.

2.2.1 Flame model

The flame model describes how fluctuations in the heat release rate, depend on the flow fluctuations induced by the acoustics just ahead of the flame.

Linear flame transfer function

For weak perturbations, the linear flame transfer function (FTF) has been used for decades to describe the linear response of heat release rate perturbations to disturbances in the velocity $\hat{u}$ or the equivalence ratio $\hat{\phi}$. The link can be mathematically expressed in the Laplace-domain:

$$\frac{\tilde{\dot{q}}(s)}{\bar{\dot{q}}} = \widetilde{\mathcal{T}}_u(s)\frac{\tilde{u}(s)}{\bar{u}} + \widetilde{\mathcal{T}}_\phi(s)\frac{\tilde{\phi}(s)}{\bar{\phi}} \tag{12}$$

where $\widetilde{\mathcal{T}}_u(s)$ and $\widetilde{\mathcal{T}}_\phi(s)$ denote the responses of the flame to velocity perturbations $\tilde{u}$ and incoming mixture inhomogeneities $\tilde{\phi}$ respectively. In this work, only the transfer function

7

$\widetilde{\mathcal{T}}_u(s)$ is accounted for. For practical combustion chambers, the impedance of the fuel feed line is generally much larger than that of the air line. When the pressure disturbances interact with the injection unit (fuel+air), only the air line will respond significantly to these disturbances. There is thus a relation between the mixture composition and velocity disturbances which can be expressed as $\tilde{\phi}/\bar{\phi} = -\tilde{u}/\bar{u}$ [7], or $\tilde{\phi}/\bar{\phi} = -k_1\tilde{u}/\bar{u}\big/(1 + k_1\tilde{u}/\bar{u})$ proposed by [8], where k_1 is a coefficient of the mixture strength model. Herein, we can express the normalized heat release rate disturbances as the function of normalized velocity perturbations in the unburned gases:

$$\frac{\tilde{\dot{q}}(s)}{\bar{\dot{q}}} = \mathcal{T}_u(s)\frac{\tilde{u}_u(s)}{\bar{u}_u} \tag{13}$$

where the subscript u denotes unburned gases.

The flame model then describes how the (normalized) unsteady heat release rate of the flame responds to (normalized) velocity fluctuations. One can choose between prescribing a flame transfer function model (with non-linearity options) or loading and fitting experimental data in the operating panel of the OSCILOS. Four kinds of flame transfer function (FTF) models can be prescribed: the first three involve (1) Crocco's famous $n - \tau$ model [9]; (2) the $n - \tau$ model filtered by a first order filter [10, 11] to capture the flame response shape for conical flames; (3) the $n - \tau$ model filtered by a second order filter [11] to capture the flame response shape for V-shape flames. These FTF models can be expressed as:

$$\mathcal{T}_{u,1}(s) = a_f e^{-\tau_f s} \tag{14a}$$

$$\mathcal{T}_{u,2}(s) = \frac{\omega_c}{s + \omega_c} a_f e^{-\tau_f s} \tag{14b}$$

$$\mathcal{T}_{u,3}(s) = \frac{\omega_c^2}{s^2 + 2\xi\omega_c s + \omega_c^2} a_f e^{-\tau_f s} \tag{14c}$$

where a_f is the gain and τ_f indicates the time delay. $\omega_c = 2\pi f_c$ denotes the cut-off frequency of the filter and ξ represents the damping coefficient of the second order low pass filter.

$$\mathcal{T}_u(s) = \frac{b_1 s^{n-1} + b_2 s^{n-2} + \cdots + b_{n-1} s + b_n}{a_1 s^{m-1} + a_2 s^{m-2} + \cdots + a_{m-1} s + a_m} \tag{15}$$

The fourth option is a user-defined FTF model using a polynomial transfer function, as shown in Eq. 15, by inputting the numerator coefficients $\mathbf{b}$ and denominator coefficients $\mathbf{a}$. The order of the numerator should not be larger than that of denominator $n \leq m$.
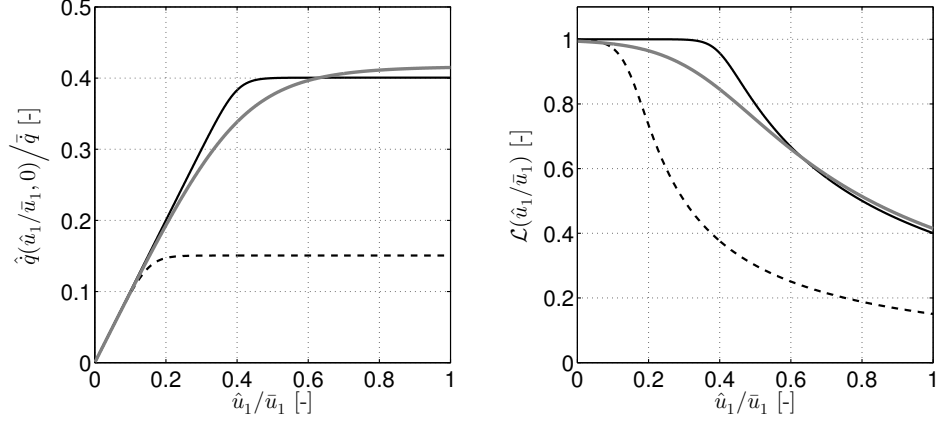
Figure 2: Three examples of the nonlinear model. Black solid line: $\alpha = 0.6$ and $\beta = 40$; gray solid line: $\alpha = 0.6$ and $\beta = 10$; dashed line: $\alpha = 0.85$ and $\beta = 40$ (this model is used in the later calculations).

Nonlinear flames

In practice, most flames feature a nonlinear response to flow disturbances [12, 13, 14, 15, 16]. Saturation of the heat release rate amplitude or a phase lag change relative to the acoustic pressure (and hence a change in the Rayleigh source term $< p'\dot{q}' >$ driving combustion instabilities [17, 18]) where the modulation level have been experimentally identified in many cases [19, 20, 15, 21].

It is clear that the linear flame transfer function is not enough to anticipate all of the characteristics of combustion instabilities; in particular it cannot predict the saturation amplitude or the time to limit cycle. Two nonlinear flame model concepts have been implemented in OSILOS, the "flame describing function" (FDF), and the G-Equation model described as follows:

- The "flame describing function" (FDF) treats the response of heat release rate as a linear regime for small perturbation levels and a weakly nonlinear regime for larger disturbance amplitudes [11, 20].

- The G-Equation model is a level set methods describing the kinematic behaviour of the flame. [23, 10, 24, 2]. It is also a weakly nonlinear flame model, and its behaviour with large flame deformations leads to saturation of the heat release rate amplitude.
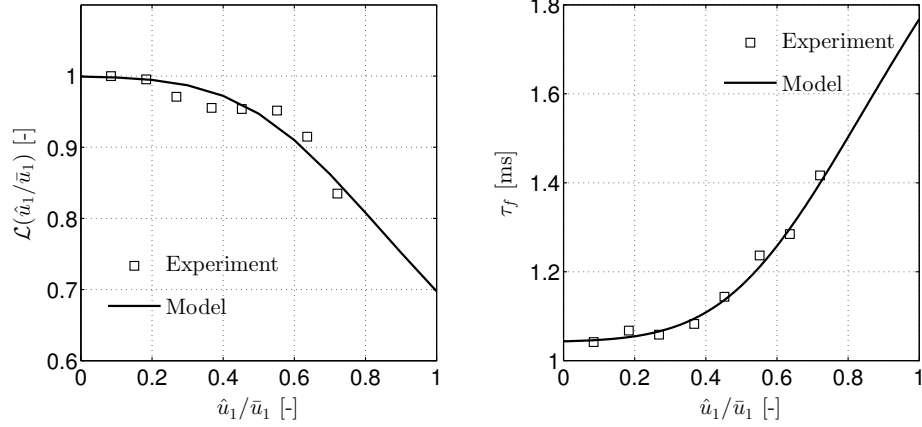
9

Figure 3: Comparison between the experimental results from Fig. 7 in [22] and t he nonlinear model ($\alpha = 0.3$, $\beta = 6$ and $\tau_f^N = 2.4$ ms). Left figure: $f = 400$ Hz, $\mathcal{L}(\hat{u}_1/\bar{u}_1) = |\widetilde{G}(\hat{u}_1/\bar{u}_1, f)|\big/|\widetilde{G}(0, f)|$. Right figure: τ_f is calculated by linear fitting of the phase for modulating frequency ranging from 0 Hz to 600 Hz.

Nonlinear flame describing functions In OSCILOS, users can choose between prescribing an analytically nonlinear flame describing function or loading and fitting experimental / CFD data. Two kinds of nonlinear flame describing functions can be prescribed: (1) an abrupt heat release rate ratio $\hat{\dot{q}}/\bar{\dot{q}}$ saturation model proposed by Dowling [11], which can be mathematically expressed as:

$$\frac{\dot{q}'}{\bar{\dot{q}}} = \begin{cases} \left(\dfrac{\dot{q}'}{\bar{\dot{q}}}\right)_L & \text{for } \left|\dfrac{\dot{q}'}{\bar{\dot{q}}}\right| \leq \alpha \\ \alpha \, \text{sgn}\left(\dfrac{\dot{q}'}{\bar{\dot{q}}}\right) & \text{else} \end{cases} \tag{16}$$

where α is a constant associated with the saturation ($0 \leq \alpha \leq 1$) and $\left(\dot{q}'\big/\bar{\dot{q}}\right)_L$ denotes the heat release rate ratio for weak perturbations, which can be calculated from the linear flame transfer function.

(2) The second nonlinear model is recently proposed by the authors [25]. The nonlinear flame describing function depends on s and velocity ratio $\hat{u}_1/\bar{u}_1$ and it is assumed here can be decoupled as:

$$\widetilde{G}(\hat{u}_1/\bar{u}_1, s) = \mathcal{L}(\hat{u}_1/\bar{u}_1)\widetilde{\mathcal{T}}_u(s) \tag{17}$$

10

where the superscript $\hat{}$ indicates the signal amplitude. The nonlinear function $\mathcal{L}(\hat{u}_1/\bar{u}_1)$ describes the saturation of heat release rate with velocity perturbations $\hat{u}_1/\bar{u}_1$, and $\mathcal{L}(\hat{u}_1/\bar{u}_1) = \widetilde{G}(\hat{u}_1/\bar{u}_1, 0)$. The mathematical link proposed in [25] is:

$$\frac{\widehat{\hat{q}}(\hat{u}_1/\bar{u}_1, 0)}{\bar{q}} = \mathcal{L}(\hat{u}_1/\bar{u}_1)\frac{\hat{u}_1}{\bar{u}_1} = \int_0^{\hat{u}_1/\bar{u}_1} \frac{1}{1 + (\xi + \alpha)^{\beta}} \mathrm{d}\xi \tag{18}$$

where α and β are two coefficients which determine the shape of the nonlinear model. Figure 2 shows 3 examples of the proposed nonlinear model. The left figure shows the evolution of heat release rate perturbation ratio $\hat{q}/\bar{q}$ with velocity disturbance level $\hat{u}_1/\bar{u}_1$ when $s = 0$, while the trajectories of the nonlinear function $\mathcal{L}$ are presented in the right figure. For weak velocity disturbances, the link between $\hat{q}/\bar{q}$ and $\hat{u}_1/\bar{u}_1$ is linear. For example, the linear region for the first case is $\hat{u}_1/\bar{u}_1 \in [0 \ \ 0.4]$, with corresponding proportional coefficient $\mathcal{L} \approx 1$ in the right figure. One may denote the upper limit of the linear region by the velocity disturbance ratio $(\hat{u}_1/\bar{u}_1)_s$. When the level of velocity disturbances exceeds $(\hat{u}_1/\bar{u}_1)_s$, $\mathcal{L}$ decreases and the heat release rate perturbations begin to saturate. It can be found that the saturation limit $(\hat{u}_1/\bar{u}_1)_s$ is mainly determined by the coefficient α; $(\hat{u}_1/\bar{u}_1)_s$ decreases as α increases towards unity. The smoothness of the saturation corner is controlled by the coefficient β. The proposed model guarantees saturation for larger velocity perturbation ratios.

One may also introduce a simple nonlinear model of the time delay, using the mathematical description:

$$\tau_f = \tau_f^0 + \tau_f^N\big(1 - \mathcal{L}(\hat{u}_1/\bar{u}_1)\big) \tag{19}$$

where τ_f^0 means the time delay when $\hat{u}_1/\bar{u}_1 = 0$ and τ_f^N is a time delay to describe the change of τ_f as $\mathcal{L}$ changes.

Figure 3 shows the comparison between the experimental matrix burner measurements and the nonlinear model. A good match is found for the evolutions of gain and time delay of the flame describing function with the increase of velocity disturbances. The exact form of the nonlinear flame model is not fully representative of a real configuration, but provides a simplified model which captures nonlinear features of real experimental flames significantly better than a simple $n - \tau$ model with abrupt saturation [26, 27] as shown in Figure 3, and thus can be used to get a better understanding of combustion instabilities.

The first order expressions linking the fresh mixture and burned gases after the flame

can be written as:

$$
\mathcal{B}_{k,2}^{\text{ii}}
\begin{bmatrix}
\tilde{p}_{k+1}(x_k,s) \\
\bar{\rho}_{k+1}\bar{c}_{k+1}\tilde{u}_{k+1}(x_k,s) \\
\tilde{\rho}_{k+1}(x_k,s)\bar{c}_{k+1}^2
\end{bmatrix}
= \mathcal{B}_{k,1a}^{\text{ii}}
\begin{bmatrix}
\tilde{p}_{k+\frac{1}{2}}(x_k,s) \\
\bar{\rho}_{k+\frac{1}{2}}\bar{c}_{k+\frac{1}{2}}\tilde{u}_{k+\frac{1}{2}}(x_k,s) \\
\tilde{\rho}_{k+\frac{1}{2}}(x_k,s)\bar{c}_k^2
\end{bmatrix}
+ \mathcal{B}_{k,1b}^{\text{ii}}
\begin{bmatrix}
\tilde{p}_k(x_k,s) \\
\bar{\rho}_k\bar{c}_k\tilde{u}_k(x_k,s) \\
\tilde{\rho}_k(x_k,s)\bar{c}_k^2
\end{bmatrix}
$$
(20a)

$$
\mathcal{B}_{k,2}^{\text{i}}
\begin{bmatrix}
\tilde{p}_{k+\frac{1}{2}}(x_k,s) \\
\bar{\rho}_{k+\frac{1}{2}}\bar{c}_{k+\frac{1}{2}}\tilde{u}_{k+\frac{1}{2}}(x_k,s) \\
\tilde{\rho}_{k+\frac{1}{2}}(x_k,s)\bar{c}_k^2
\end{bmatrix}
= \mathcal{B}_{k,1}^{\text{i}}
\begin{bmatrix}
\tilde{p}_k(x_k,s) \\
\bar{\rho}_k\bar{c}_k\tilde{u}_k(x_k,s) \\
\tilde{\rho}_k(x_k,s)\bar{c}_k^2
\end{bmatrix}
$$
(20b)

where,

$$
\mathcal{B}_{k,2}^{\text{ii}} =
\begin{bmatrix}
0 & 1 & \bar{M}_{k+1} \\[2mm]
1 & 2\bar{M}_{k+1} & \bar{M}_{k+1}^2 \\[2mm]
\dfrac{\gamma_2}{\gamma_2-1}\dfrac{\bar{c}_{k+1}}{\bar{c}_{k+\frac{1}{2}}}\bar{M}_{k+1} & \dfrac{\bar{c}_{k+1}}{\bar{c}_{k+\frac{1}{2}}}\bar{M}_{k+1}^2 & -\dfrac{1}{\gamma_2-1}\dfrac{\bar{c}_{k+1}}{\bar{c}_{k+\frac{1}{2}}}\bar{M}_{k+1}
\end{bmatrix}
$$
(21a)

$$
\mathcal{B}_{k,1a}^{\text{ii}} =
\begin{bmatrix}
0 & \dfrac{\bar{c}_{k+1}}{\bar{c}_{k+\frac{1}{2}}} & \bar{M}_{k+\frac{1}{2}}\dfrac{\bar{c}_{k+1}}{\bar{c}_{k+\frac{1}{2}}} \\[3mm]
1 & 2\bar{M}_{k+\frac{1}{2}} & \bar{M}_{k+\frac{1}{2}}^2 \\[3mm]
\dfrac{\gamma_1}{\gamma_1-1}\bar{M}_{k+\frac{1}{2}} & \bar{M}_{k+\frac{1}{2}}^2 - \dfrac{\Delta H}{\bar{c}_{k+\frac{1}{2}}^2} & -\bar{M}_{k+\frac{1}{2}}\left(\dfrac{1}{\gamma_1-1}+\dfrac{\Delta H}{\bar{c}_{k+\frac{1}{2}}^2}\right)
\end{bmatrix}
$$
(21b)

$$
\mathcal{B}_{k,1b}^{\text{ii}} =
\begin{bmatrix}
0 & 0 & 0 \\[2mm]
0 & 0 & 0 \\[2mm]
0 & \dfrac{\Delta H}{\Theta_k\bar{c}_k\bar{c}_{k+\frac{1}{2}}}\widetilde{\mathcal{G}}_u & 0
\end{bmatrix}
$$
(21c)

$$
\mathcal{B}_{k,2}^{\mathrm{i}} = \Theta_k
\begin{bmatrix}
0 & 1 & \bar{M}_{k+\frac{1}{2}} \\[2ex]
1 & 2\bar{M}_{k+\frac{1}{2}} & \bar{M}_{k+\frac{1}{2}}^2 \\[2ex]
\dfrac{\gamma_1}{\gamma_1 - 1}\dfrac{\bar{c}_{k+\frac{1}{2}}}{\bar{c}_k}\bar{M}_{k+\frac{1}{2}} & \dfrac{\bar{c}_{k+\frac{1}{2}}}{\bar{c}_k}\bar{M}_{k+\frac{1}{2}}^2 & -\dfrac{1}{\gamma_1 - 1}\dfrac{\bar{c}_{k+\frac{1}{2}}}{\bar{c}_k}\bar{M}_{k+\frac{1}{2}}
\end{bmatrix}
\tag{22a}
$$

$$
\mathcal{B}_{k,1}^{\mathrm{i}} =
\begin{bmatrix}
0 & \dfrac{\bar{c}_{k+\frac{1}{2}}}{\bar{c}_k} & \bar{M}_k\dfrac{\bar{c}_{k+\frac{1}{2}}}{\bar{c}_k} \\[2ex]
\Theta_k & 2\bar{M}_k & \bar{M}_k^2 \\[2ex]
\dfrac{\gamma_1}{\gamma_1 - 1}\bar{M}_k & \bar{M}_k^2 & -\dfrac{1}{\gamma_1 - 1}\bar{M}_k
\end{bmatrix}
\tag{22b}
$$

Equation 20 can be changed to:

$$
\mathcal{B}_{k,2}^{\mathrm{ii}}
\begin{bmatrix}
\tilde{p}_{k+1}(x_k,s) \\[1ex]
\bar{\rho}_{k+1}\bar{c}_{k+1}\tilde{u}_{k+1}(x_k,s) \\[1ex]
\tilde{\rho}_{k+1}(x_k,s)\bar{c}_{k+1}^2
\end{bmatrix}
= \left(\mathcal{B}_{k,1a}^{\mathrm{ii}}\left(\mathcal{B}_{k,2}^{\mathrm{i}}\right)^{-1}\mathcal{B}_{k,1}^{\mathrm{i}} + \mathcal{B}_{k,1b}^{\mathrm{ii}}\right)
\begin{bmatrix}
\tilde{p}_k(x_k,s) \\[1ex]
\bar{\rho}_k\bar{c}_k\tilde{u}_k(x_k,s) \\[1ex]
\tilde{\rho}_k(x_k,s)\bar{c}_k^2
\end{bmatrix}
\tag{23}
$$

In case there is no area change at the flame position, $\left(\mathcal{B}_{k,2}^{\mathrm{i}}\right)^{-1}\mathcal{B}_{k,1}^{\mathrm{i}} = \mathbf{I}_3$, where $\mathbf{I}_3$ is an dentity matrix.

The array of linearised flow variables $\tilde{p}(s)$, $\bar{\rho}\bar{c}\tilde{u}(s)$ and $\tilde{\rho}(s)\bar{c}^2$ can be expressed as the function of the wave strengths $\widetilde{A}^+$, $\widetilde{A}^-$ and $\widetilde{E}$:

$$
\begin{bmatrix}
\tilde{p}_{k+1}(x_k,s) \\[1ex]
\bar{\rho}_{k+1}\bar{c}_{k+1}\tilde{u}_{k+1}(x_k,s) \\[1ex]
\tilde{\rho}_{k+1}(x_k,s)\bar{c}_{k+1}^2
\end{bmatrix}
= \mathcal{C}_2\mathcal{D}_{k,2}(s)
\begin{bmatrix}
\widetilde{A}_{k+1}^+(s) \\[1ex]
\widetilde{A}_{k+1}^-(s) \\[1ex]
\widetilde{E}_{k+1}(s)
\end{bmatrix}
\tag{24a}
$$

$$
\begin{bmatrix}
\tilde{p}_k(x_k,s) \\[1ex]
\bar{\rho}_k\bar{c}_k\tilde{u}_k(x_k,s) \\[1ex]
\tilde{\rho}_k(x_k,s)\bar{c}_k^2
\end{bmatrix}
= \mathcal{C}_1\mathcal{D}_{k,1}(s)
\begin{bmatrix}
\widetilde{A}_k^+(s) \\[1ex]
\widetilde{A}_k^-(s) \\[1ex]
\widetilde{E}_k(s)
\end{bmatrix}
\tag{24b}
$$

13

where

$$\mathcal{C}_1 = \mathcal{C}_2 = \begin{bmatrix} 1 & 1 & 0 \\ 1 & -1 & 0 \\ 1 & 1 & -1 \end{bmatrix} \tag{25}$$

$$\mathcal{D}_{k,1}(s) = \begin{bmatrix} e^{-\tau_k^+ s} & & \\ & 1 & \\ & & e^{-\tau_k^s s} \end{bmatrix} \qquad \mathcal{D}_{k,2}(s) = \begin{bmatrix} 1 & & \\ & e^{-\tau_{k+1}^- s} & \\ & & 1 \end{bmatrix} \tag{26}$$

Thus:

$$\begin{bmatrix} \widetilde{A}_{k+1}^+(s) \\ \widetilde{A}_{k+1}^-(s) \\ \widetilde{E}_{k+1}(s) \end{bmatrix} = \mathcal{Z}_k(s) \begin{bmatrix} \widetilde{A}_k^+(s) \\ \widetilde{A}_k^-(s) \\ \widetilde{E}_k(s) \end{bmatrix} \tag{27}$$

where

$$\mathcal{Z}_k(s) = \left(\mathcal{D}_{k,2}(s) \right)^{-1} \left(\mathcal{B}_{k,2}\mathcal{C}_2 \right)^{-1} \mathcal{B}_{k,1}\mathcal{C}_1\mathcal{D}_{k,1}(s) \tag{28}$$

The global matrix $\mathcal{G}_{k,k}$ integrates all interfaces from k to j:

$$\mathcal{G}_{k,j}(s) = \mathcal{Z}_k(s)\mathcal{Z}_{k-1}(s)\ldots\mathcal{Z}_k(s) \tag{29}$$

The link between magnitudes of the acoustic waves and entropy waves at the inlet of the combustor ($\widetilde{A}_1^+(s)$, $\widetilde{A}_1^-(s)$ and $\widetilde{E}_1(s)$) and those at the outlet ($\widetilde{A}_N^+(s)$, $\widetilde{A}_N^-(s)$ and $\widetilde{E}_N(s)$) can be expressed as:

$$\begin{bmatrix} \widetilde{A}_N^+(s) \\ \widetilde{A}_N^-(s) \\ \widetilde{E}_N(s) \end{bmatrix} = \mathcal{G}_{1,N-1}(s) \begin{bmatrix} \widetilde{A}_1^+(s) \\ \widetilde{A}_1^-(s) \\ \widetilde{E}_1(s) \end{bmatrix} \tag{30}$$

14

G-Equation The G-Equation is implemented in its single valued flame tracking form in OSCILOS, which is a valid approach for small perturbation velocities $\hat{u}_1$ [28]. The heat source is set at a position x_k.

We define a non-reacting scalar $G(\mathbf{x}, t)$ in an axisymmetric combustor. We choose to represent the flame surface with the iso-scalar $G(\mathbf{x}, t) = G_0$, such that $G(\mathbf{x}, t) < G_0$ represents the unburnt fluid, and $G(\mathbf{x}, t) > G_0$ represents the burnt fluid. This is shown in figure 4. As the motion of the flame front is represented by the motion of the surface defined by the iso-scalar G_0, we can describe the position of the flame front through the material derivative $\frac{DG}{Dt}$ when $G(\mathbf{x}, t) = G_0$. We know that the flame is convected by the duct flow $\mathbf{u}_{\mathrm{gutter}}$ present right before the flame (the bold font indicating its vector form), and the laminar burning velocity S_u of the flame. Expressing this in the material derivative yields:

$$\frac{DG}{Dt} = \frac{\partial G}{\partial t} + (\mathbf{u}_{\mathrm{gutter}} - S_u\mathbf{n}) \cdot \nabla G = 0 \tag{31}$$

where S_u is the speed of propagation of a laminar flat flame surface into unburnt gas, and $\mathbf{n}$ is the normal to the flame surface pointing towards the burnt gas. By expressing the normal as $\mathbf{n} = \frac{\nabla G}{|\nabla G|}$, and using this in the expression above, we obtain the well known multivalued G-Equation form [23]:

$$\frac{\partial G}{\partial t} = -\mathbf{u}_{\mathrm{gutter}} \cdot \nabla G + S_u|\nabla G| \tag{32}$$

We choose to simplify the problem to the case of a single valued flame, under the assumption of small incoming perturbations [28]. To do this we track the flame by writing $G(\mathbf{x}, t) - G_0 = (x - x_a) - \xi(r, t)$ where $\xi(r, t)$ is a single valued function which depends only on r and time [10, 24]. Using this in (32), and noting that only axial duct flow is present under the plane wave assumption, yields the simpler flame-front tracking version of the G-Equation which is implemented in OSCILOS:

$$\frac{\partial \xi}{\partial t} = u_{\mathrm{gutter}} - S_u\sqrt{1 + \left(\frac{\partial \xi}{\partial r}\right)^2} \tag{33}$$

As the behaviour of the flame remains symmetric, all of the following derivations will be presented for the top half of the duct only. Furthermore, we will assume that the laminar burning velocity S_u remains an empirical constant, and does not depends on the curvature of the flame. The value of S_u can be set by the user in the OSCILOS GUI.

In the configuration presented in OSCILOS, the flame remains anchored to a flame holder positioned on the centerline of the duct at a position x_a. When choosing the location x_k of the heat release source for a G-Equation flame in OSCILOS, the user is effectively choosing the anchor location x_a, and we set the initial condition $\xi(r_a, 0) = x_a$
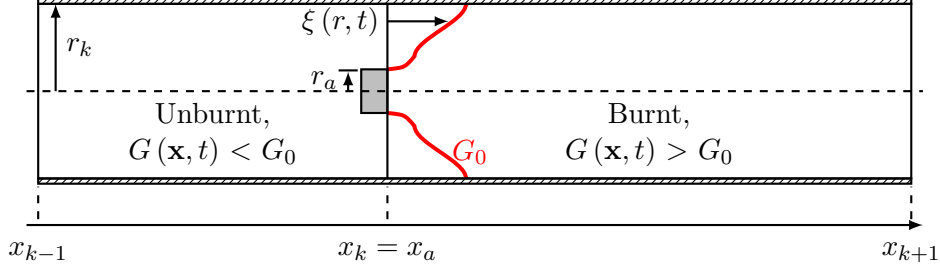
15

Figure 4: Diagram of the G-Equation flame in the duct.

where r_a corresponds to the radius of the flame holder [24]. The anchoring of the flame on the flame holder is imposed by:

$$\begin{cases} \frac{\partial \xi}{\partial t}(r_a, t) = 0 \text{ for } \xi(r_a, t) \geq x_a \\ \frac{\partial \xi}{\partial r}(r_a, t) = 0 \text{ for } \xi(r_a, t) < x_a \end{cases} \tag{34}$$

where ξ is define for $r_a \leq r \leq r_k$. These condition model the fact that anchoring of the flame only occurs if the flame reaches the downstream face of the flame holder.

The first condition of (34) leads from (33) to the imposed gradient $\frac{\partial \xi}{\partial r}(r_a, t) = \sqrt{\left(\frac{u_{\text{gutter}}}{S_u}\right)^2 - 1}$ at $r = r_a$ when $|u_{\text{gutter}}| \geq |S_u|$. When the acoustic perturbations are such that $|u_{\text{gutter}}| < |S_u|$, the flame is allowed to move freely backwards as would occur during a flashback, and we impose $\frac{\partial \xi}{\partial r}(r_a, t) = 0$.

The flame anchor occupies a finite volume within the duct. Even though we continue to assume plane wave acoustics in the area of the flame holder, we do take into account a local acceleration of the axial flow due to blockage effects. As such, we can obtain the axial velocity in the gutter, directly affecting the flame, from $u_{\text{gutter}} = (\bar{u}_1 + \hat{u}_1) / \left(1 - (r_a/r_k)^2\right)$, where the fluctuating and mean axial velocity are taken just before x_a.

The steady solution of the flame is obtained by writing $\frac{\partial \bar{\xi}}{\partial t} = 0$, which leads to the constant gradient in the upper half of the duct $\frac{\partial \bar{\xi}}{\partial r} = \sqrt{\left(\frac{\bar{u}_{\text{gutter}}}{S_u}\right)^2 - 1}$ (the bar indicating the steady part). Note that a physical steady solution does not exist if $\bar{u}_{\text{gutter}} < S_u$. With the initial condition at the anchoring point $\xi(r_a, 0) = x_a$, this yields the steady solution for the flame:

$$\bar{\xi}(r, t) = (r - r_a) \sqrt{\left(\frac{\bar{u}_{\text{gutter}}}{S_u}\right)^2 - 1} \tag{35}$$

It is assumed that the heat release rate of the flame is proportional to the area of the flame A_{flame}. As such, we can write that $q(t) = \bar{\rho}_1 S_u A_{\text{flame}}(t - \tau_f) \Delta_H$ [24, 29, 30] where

16

the total flame area A_{flame} (for both the top and bottom parts of the duct) is given by:

$$A_{\text{flame}}(t) = \int_{r_a}^{r_k} 2\pi r \sqrt{1 + \left(\frac{\partial \xi}{\partial r}\right)^2} \, dr \tag{36}$$

In a duct with a length downstream of the flame $x_{k+1} - x_k$, τ_f is obtained from $\tau_f = \frac{\tau_{factor}(x_{k+1} - x_k)}{\bar{u}_{\text{gutter}}}$ and represents the time taken for a perturbation at the base of the flame to propagate along the flame and affect the heat release rate. The factor τ_{factor} is chosen empirically, and can be set by the user in the OSCILOS GUI. Thus at any point in time, the heat release rate and therefore the jump in the wave amplitude either side of the flame depends on the flame area and hence the instantaneous flame shape.

The numerical implementation of the G-Equation in OSCILOS is done using a finite difference methods. The gradient term is obtained using a first order backward Euler method, with the boundary condition providing the value of the gradient for $r = r_a$. Time integration of the G-Equation in OSCILOS has been implemented with both an explicit first order Euler method, and an Adam-Bashforth three step third order method (selected by default).

When selecting the G-Equation, the value of u_{gutter} is computed from the pressure waves A_k^- and A_k^+ at each time step. This allows for the new flame shape and heat release rate ratio to be obtained, and for the pressure waves and entropy waves along the duct to be recomputed at each iteration. When dealing with multiple heat source, all heat sources must currently be using G-Equation models; this is due to the limitations imposed by the time integration of the G-Equation.

2.2.2 Advection of entropy waves

For low Mach number situations, the entropy waves vary rapidly along the longitudinal direction and hence are likely to undergo shear dispersion in long chambers. We thus account for the attenuation of the entropy waves over the long chamber and $\mathcal{C}_1$ can be changed to:

$$\mathcal{C}_1 = \begin{bmatrix} 1 & 1 & 0 \\ 1 & -1 & 0 \\ 1 & 1 & 0 \end{bmatrix} \tag{37}$$

For large Mach number situations, at the combustor exit (choked end) / turbine inlet, the entropy waves are subjected to a rapid flow acceleration due to the significant cross sectional area convergence, and this results in the generation of acoustic waves, as first described by [31]. These acoustic waves are termed 'entropy noise' or 'indirect combustion

17

noise'. The upstream-propagating component affects the flame within the combustor, and thus can influence thermoacoustic stability [32, 7]. Between the flame, where they are generated, and the combustor exit/turbine inlet, where they are accelerated, entropy waves are subject to advection by a flow that has both a non-uniform mean spatial profile (for example, a fully developed profile) and turbulent fluctuations. Two models accounting for the advection of entropy waves are prescribed in this work. These models considered the impulse response at locations downstream of the flame within a combustor. The impulse response is the time variation of the entropy perturbation (averaged over cross-section) that arises from an impulse, $\delta(t)$, applied at the combustor inlet, nominally the flame location. This corresponds to the probability density function (p.d.f.) of the 'residence time' of a particle advecting from the inlet to the outlet. The model options for the shear dispersion effects are:

- A "Rectangular" model (proposed by Sattelmayer [33]): The p.d.f. or impulse response is modelled as a rectangular pulse of length $2\Delta\tau_C^s$ and height $1/2\Delta\tau_C^s$ centred about the mean residence time τ_C^s:

$$E_C^{\text{inlet}}(t) = \delta(t) \tag{38a}$$

$$E_C^{\text{outlet}}(t) = \begin{cases} \dfrac{1}{2\Delta\tau_C^s} & \text{for } \tau_C^s - \Delta\tau_C^s \leq t \leq \tau_C^s + \Delta\tau_C^s \\ 0 & \text{else} \end{cases} \tag{38b}$$

The corresponding Laplace transform of the transfer function between the entropy waves at the outlet and inlet can be expressed as:

$$\frac{\widetilde{E}_C^{\text{outlet}}(s)}{\widetilde{E}_C^{\text{inlet}}(s)} = \widetilde{\mathcal{E}}(s) \exp\left(-\tau_C^s\, s\right) = \frac{\exp\left(\Delta\tau_C^s\, s\right) - \exp\left(-\Delta\tau_C^s\, s\right)}{2\Delta\tau_C^s\, s} \exp\left(-\tau_C^s\, s\right) \tag{39}$$

with the Fourier transforms of the transfer function:

$$\widetilde{\mathcal{E}}(i\omega) = \text{sinc}\left(i\omega\Delta\tau_C^s\right) \tag{40}$$

where the function $\text{sinc}(x) = \sin(x)/x$.

- A "Gaussian" model (proposed by Morgans et al. [34]): Shear dispersion is assumed to be predominantly caused by spatial variations in the time-mean velocity profile, rather than by turbulent eddies. DNS simulations of a channel flow show that the p.d.f. exhibits a Gaussian-like shape with extended back-foot. The impulse response is modelled as a Gaussian distribution:

$$E_C^{\text{inlet}}(t) = \delta(t) \tag{41a}$$

$$E_C^{\text{outlet}}(t) = A_\delta \exp\left(-\pi A_\delta^2\left(t - \tau_C^s\right)^2\right) \tag{41b}$$

A time delay $\Delta\tau_C^s$ is also proposed to describe the dispersion of resident time using the definition:

$$E_C^{\text{outlet}}(\tau_C^s + \Delta\tau_C^s) = A_\delta \exp\left(-\pi A_\delta^2 \left(\Delta\tau_C^s\right)^2\right) = A_\delta \exp(-1) \tag{42}$$

A_δ thus can be expressed as the function of $\Delta\tau_C^s$:

$$A_\delta = \frac{1}{\sqrt{\pi}\Delta\tau_C^s} \tag{43}$$

Equation 41b can be changed to:

$$E_C^{\text{outlet}}(t) = \frac{1}{\sqrt{\pi}\Delta\tau_C^s} \exp\left(-\left(\frac{t - \tau_C^s}{\Delta\tau_C^s}\right)^2\right) \tag{44}$$

with the Fourier transforms of the transfer function:

$$\widetilde{\mathcal{E}}(i\omega) = \exp\left(-\frac{\left(\omega\Delta\tau_C^s\right)^2}{4}\right) \tag{45}$$

For causal systems, the Fourier and Laplace transforms are the same and the above Fourier transform are changed to the Laplace transform by replacing $i\omega$ by the Laplace variable s, which yields:

$$\widetilde{\mathcal{E}}(s) = \exp\left(\frac{\left(\Delta\tau_C^s\, s\right)^2}{4}\right) \tag{46}$$

The coefficient $\mathcal{D}_{k,1}(s)$ in the combustor section in this situation thus should be changed to:

$$\mathcal{D}_{C,1}(s) = \begin{bmatrix} e^{-\tau_C^+ s} & & \\ & 1 & \\ & & k_d\widetilde{\mathcal{E}}(s)e^{-\tau_C^s s} \end{bmatrix} \tag{47}$$

where $k_d \leq 1$, is a dissipative factor to account for the fact that the integrated strength of an entropy wave is reduced [7].

3 Boundary conditions

The link between the outward and inward propagating waves at the end of the combustor can be described by the reflection coefficients. When the indirect noise induced by the entropy waves can be neglected, the pressure reflection coefficients at the inlet and outlet are characterized by R_1 and R_2 respectively:

$$\widetilde{R}_1(s) = \frac{\widetilde{A}_1^+(s)}{\widetilde{A}_1^-(s)e^{-\tau_1^- s}} \tag{48a}$$

$$\widetilde{R}_2(s) = \frac{A_N^-(s)}{A_N^+(s)e^{-\tau_N^+ s}} \tag{48b}$$

The compressor exit and turbine inlet of a gas turbine or an aeronautic engine can be considered as a choked inlet and choked outlet respectively. The sections before and after the choked interface can be considered as independent systems. One can treat the choked interface as a boundary for the analysis of instabilities.

- Compact choked inlet: Stow et al. [35] found that for one-dimensional disturbances, perturbations in mass flux and energy flux are zero just after the shock and we have the mathematical expressions:

$$\rho_1' \bar{c}_1^2 + \frac{\bar{\rho}_1 \bar{c}_1 u_1'}{\bar{M}_1} = 0 \tag{49a}$$

$$\frac{\gamma_1 p_1'}{\gamma_1 - 1} - \frac{\rho_1' \bar{c}_1^2}{\gamma_1 - 1} + \bar{M}_1 \bar{\rho}_1 \bar{c}_1 u_1' = 0 \tag{49b}$$

The reflection coefficients can be obtained by combining the above two equations:

$$\widetilde{R}_1(s) = \frac{1 - \gamma_1 \bar{M}_1 / \left(1 + (\gamma_1 - 1)\bar{M}_1^2\right)}{1 + \gamma_1 \bar{M}_1 / \left(1 + (\gamma_1 - 1)\bar{M}_1^2\right)} \tag{50}$$

- Compact choked outlet: Marble and Candel [31] showed that the boundary condition at a compact choked outlet can be expressed as:

$$\rho_N' \bar{c}_N^2 + \frac{2\bar{\rho}_N \bar{c}_N u_N'}{\bar{M}_N} - \gamma_2 p_N' = 0 \tag{51}$$

which can be simplified to the function of $\widetilde{A}_N^+$, $\widetilde{A}_N^-$ and $\widetilde{E}_N$:

$$\widetilde{A}_N^-(s) = \widetilde{R}_2(s)\widetilde{A}_N^+(s)\exp(-\tau_N^+ s) + k_d \widetilde{R}_s(s)\widetilde{E}_N(s)\widetilde{\mathcal{E}}(s)\exp(-\tau_N^s s) \tag{52a}$$

$$\widetilde{R}_2(s) = \frac{1 - (\gamma_2 - 1)\bar{M}_N/2}{1 + (\gamma_2 - 1)\bar{M}_N/2} \tag{52b}$$

$$\widetilde{R}_s(s) = -\frac{\bar{M}_N/2}{1 + (\gamma_2 - 1)\bar{M}_N/2} \tag{52c}$$

Users can also define the reflection coefficient as a polynomial transfer function, as shown in Eq. 53, by inputting the numerator coefficients **b** and denominator coefficients **a**. The order of the numerator should not be larger than that of denominator $n \leq m$.

$$\widetilde{R}(s) = \frac{b_1 s^{n-1} + b_2 s^{n-2} + \cdots + b_{n-1}s + b_n}{a_1 s^{m-1} + a_2 s^{m-2} + \cdots + a_{m-1}s + a_m} \tag{53}$$

4   Validation and test cases

Validation of the code without damping devices has been carried out for two cases. The first case is a cold tube without heat addition and the second one is an unstable laboratory combustor.

4.1   Cold tube without heat addition

It is worth firstly discussing the situation without heat addition, such that the thermo-dynamic properties in the tube are uniform and we solve for the purely acoustic (rather than thermoacoustic) modes. The tube has a length of $l = 1$ m. The mean pressure, temperature and Mach number in the tube are $\bar{p} = 1$ bar, $\bar{T} = 300$ K and $\bar{M} = 0.001$. The inlet of the tube is a rigid wall (i.e. a closed end) and the outlet is open to the atmosphere and radiation at the end is neglected. The pressure reflection coefficients at the inlet and outlet are $R_1 = 1$ and $R_2 = -1$ respectively, which corresponds to:

$$u'(0,t) = 0 \tag{54a}$$
$$p'(l,t) = 0 \tag{54b}$$

The theoretical resonant frequency can be found from the following equation [6]:

$$\cos(2\pi fl/\bar{c}) = 0 \tag{55}$$
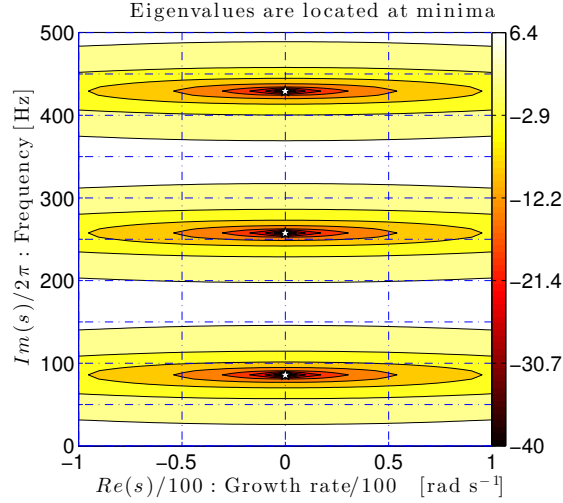
Figure 5: Contour map of $20\log_{10}|\delta e(s)|$ in the s-plane. The first three resonant frequencies indicated by the marker $\star$ are 85.8 Hz, 257.4 Hz and 429.1 Hz respectively.

with solutions:

$$f_n = \frac{2n-1}{4}\frac{\bar{c}}{l} \tag{56}$$

for integer $n \geq 1$. The first three resonant frequencies are 85.8 Hz, 257.4 Hz and 429.1 Hz respectively by substituting the mean speed of sound $\bar{c} = 343.25$ m/s into the above equation. Moreover, it also possible to deduce the corresponding mode shapes:

$$\hat{p}(x) = P_n \cos\left((2n-1)\pi x/(2l)\right) \tag{57a}$$

$$\hat{u}(x) = iP_n/(\bar{\rho}\bar{c})\sin\left((2n-1)\pi x/(2l)\right) \tag{57b}$$

for an arbitrary constant P_n.

In OSCILOS, we set $\widetilde{A}_1^-(s) = 1$ and $\widetilde{E}_1(s) = 0$ at the inlet of the combustor. To satisfy the boundary condition, $\widetilde{A}_1^+(s) = \widetilde{R}_1(s)\widetilde{A}_1^-(s)\exp(-\tau_1^+ s)$. By guessing a Laplace variable s, we can calculate the values of $\widetilde{A}_N^+(s)e^{-\tau_N^+ s}$, $\widetilde{A}_N^-(s)$ and $\widetilde{E}_N(s)e^{-\tau_N^s s}$ from the equation 30. The error at the outlet boundary can be mathematically expressed as:

$$\delta e(s) = \widetilde{A}_N^-(s) - \widetilde{R}_2(s)\widetilde{A}_N^+(s)\exp(-\tau_N^+ s) - k_d\widetilde{R}_s(s)\widetilde{E}_N(s)\widetilde{\mathcal{E}}(s)\exp(-\tau_N^s s) \tag{58}$$

It is possible to plot the contour map of $20\log_{10}|\delta e(s)|$ (as shown in Fig 5), in which the eigenvalues are located at minima. The resonant frequencies obtained from OSCILOS are
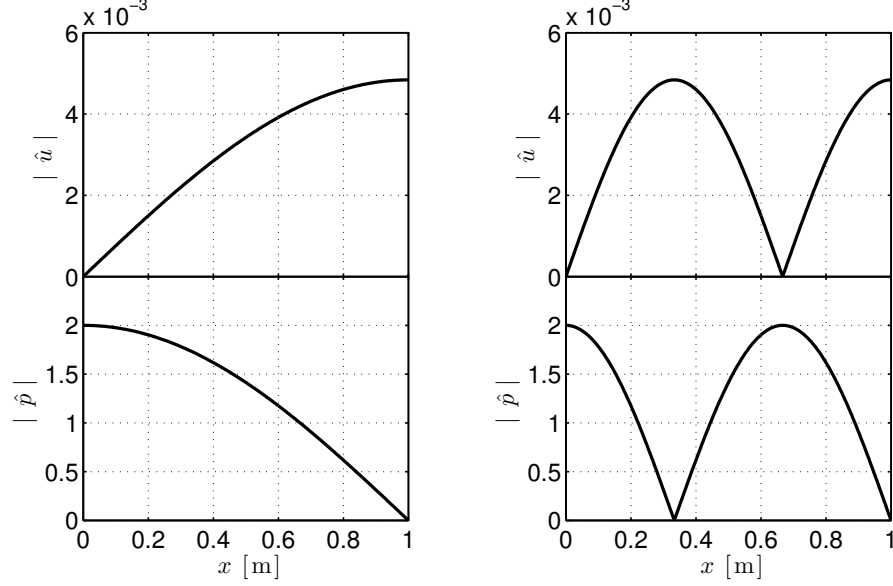
22

Figure 6: Plots of the mode shapes of the first and second modes.

the same as those from theoretical prediction. Once the eigenvalues are determined, the mode shapes can be also obtained from OSCILOS. Figure 6 shows the mode shapes of the first two modes. These plots still match well with those predicted from eqs 57a and 57b.

4.2 Unstable laboratory combustor

We now consider the case with an unstable flame. The experiments were carried out by Palies and co-workers in Laboratory EM2C [36]. The combustor includes a plenum, an injection unit and a combustion chamber terminated by an open end. The compact flame is stabilized at the beginning of the combustion chamber. Experiments were carried out for the plenum and chamber with different lengths to vary the eigenvalues of the combustor. Herein, we only take one unstable case for comparison between the predictions from OSCILOS and the experimental results.

The plenum comprises a straight cylindrical container with a length of 224 mm and a diameter of 65 mm, and a smoothly convergent cylindrical unit with a length of 60 mm. The diameters of the inlet and outlet are 60 mm and 35 mm, respectively. The injection unit has a length of 56 mm and a diameter of 22 mm. The length and diameter of the combustion chamber are 400 mm and 70 mm, respectively. More details can be found in
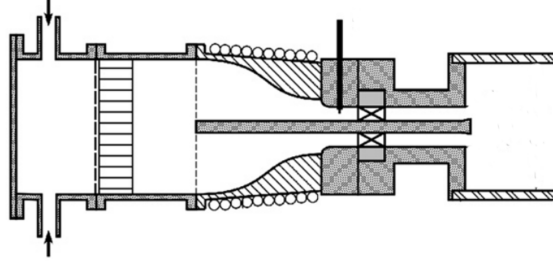
(a) Swirled configuration from Ref [36].
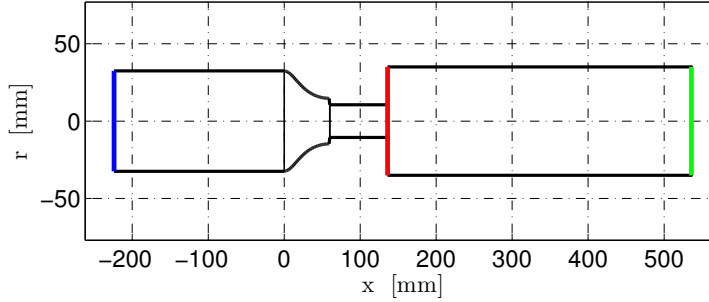
(b) Preview in OSCILOS.

Figure 7: Schematic view of the combustor.

[37]. The mean velocity at the outlet of the injection unit is $\bar{u}_2 = 4.13$ m/s. The mean pressure is $\bar{p}_1 = 1$ bar and the mean temperature is $\overline{T}_1 = 300$ K. Methane is used as the fuel and the equivalence ratio is $\phi = 0.7$. The measured mean temperature of the burned gases is 1600 K. So that the calculated mean temperature matches the experimental result, the combustion efficiency η is set to 0.825. It is thus possible to calculate the mean thermal properties and mean flows in different sections. Figure 8 shows the plots of the mean velocity $\bar{u}$ and mean temperature $\overline{T}$ in different sections. $\overline{T}_3 = 1601$ K and $\overline{T}_1 = \overline{T}_2 = 300$ K. The inlet can be considered as a rigid wall with $R_1 = 0.98$ to account for acoustic losses within the plenum. The outlet of the combustion chamber is open to atmosphere with $R_2 = -1$.

The flame describing function is loaded from the experimental data. A fitting procedure is carried out first in OSCILOS in order to determine a mathematical form from the FDF. Figure 9 shows the comparison of the experimental and fitted flame describing function. The fitted transfer function has a order of 40 and captures the shape of FTF for the most "dangerous" frequency range (0 - 400 Hz) where combustion instability may

occur. The ratio of signal amplitude to mean value $\hat{u}_u/\bar{u}_u$ is used as the normalized velocity perturbation, instead of the ratio of RMS value to mean value $u_{u,\text{rms}}/\bar{u}_u$ used in [36, 37]. By substituting the fitted FDF into the governing equations 30, one can obtain the evolutions of the eigenvalues with the velocity perturbations. Figure 10 shows the contour maps of $20 \lg |\delta e(s)|$ in the s-plane for the four normalized velocity perturbations. For weak velocity perturbation (such as Fig. 10(a)), the growth rate of the main mode is 22.2 rad s^{-1}, meaning that the system is unstable and disturbances oscillate at the corresponding eigenfrequency 131 Hz. With increasing flow velocity perturbations, the growth rate decreases (see the evolution of the main mode's growth rate in 10(b)-(d)), and a limit cycle is finally established between normalized velocity perturbations of 0.679 and 0.848. Figure 11 shows the evolution of eigenfrequency and corresponding growth rate with the normalized flow velocity perturbations. With increasing flow velocity disturbances, both the eigenfrequency and the growth rate decrease. One can predict the normalized velocity perturbation at which a limit cycle is established based on a linear interpolation, for which the growth rate is zero, here 0.714. The eigenfrequency of the final perturbations is 126.1 Hz. These match quite well the experimental results of 0.68 and 126 Hz respectively.
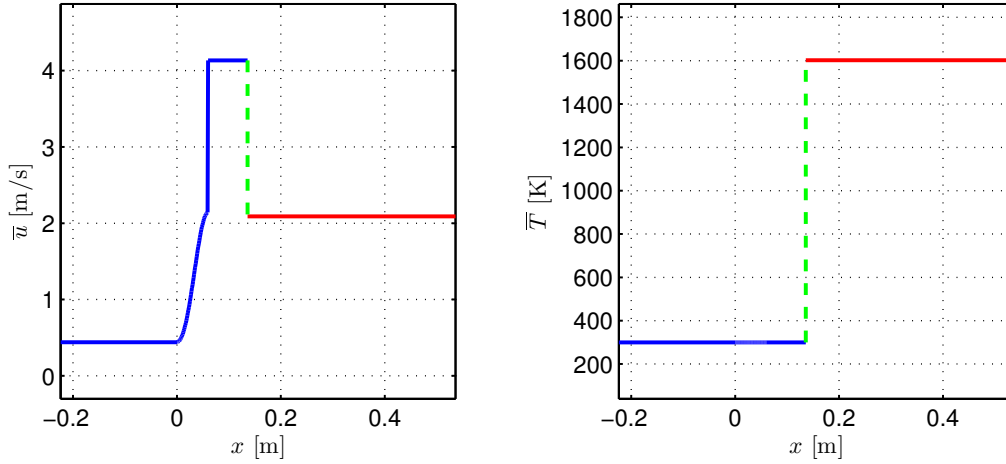

Figure 8: Plots of the mean velocity $\bar{u}$ (left figure) and the mean temperature $\bar{T}$ (right figure) in different sections.
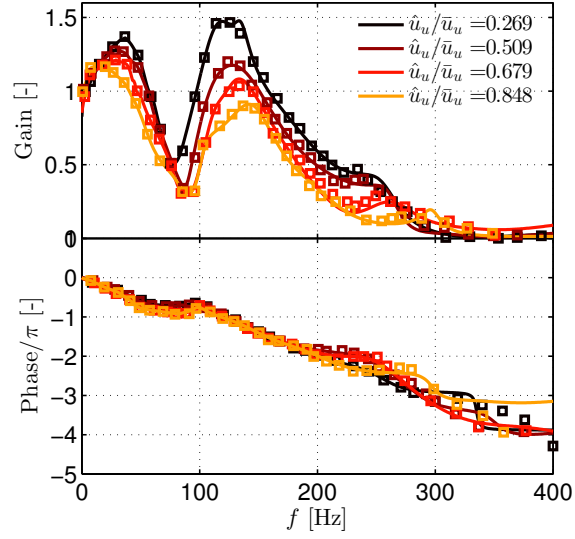
Figure 9: Comparison of the experimental (markers) and fitted (continuous line) flame describing function for different normalized velocities before the flame.
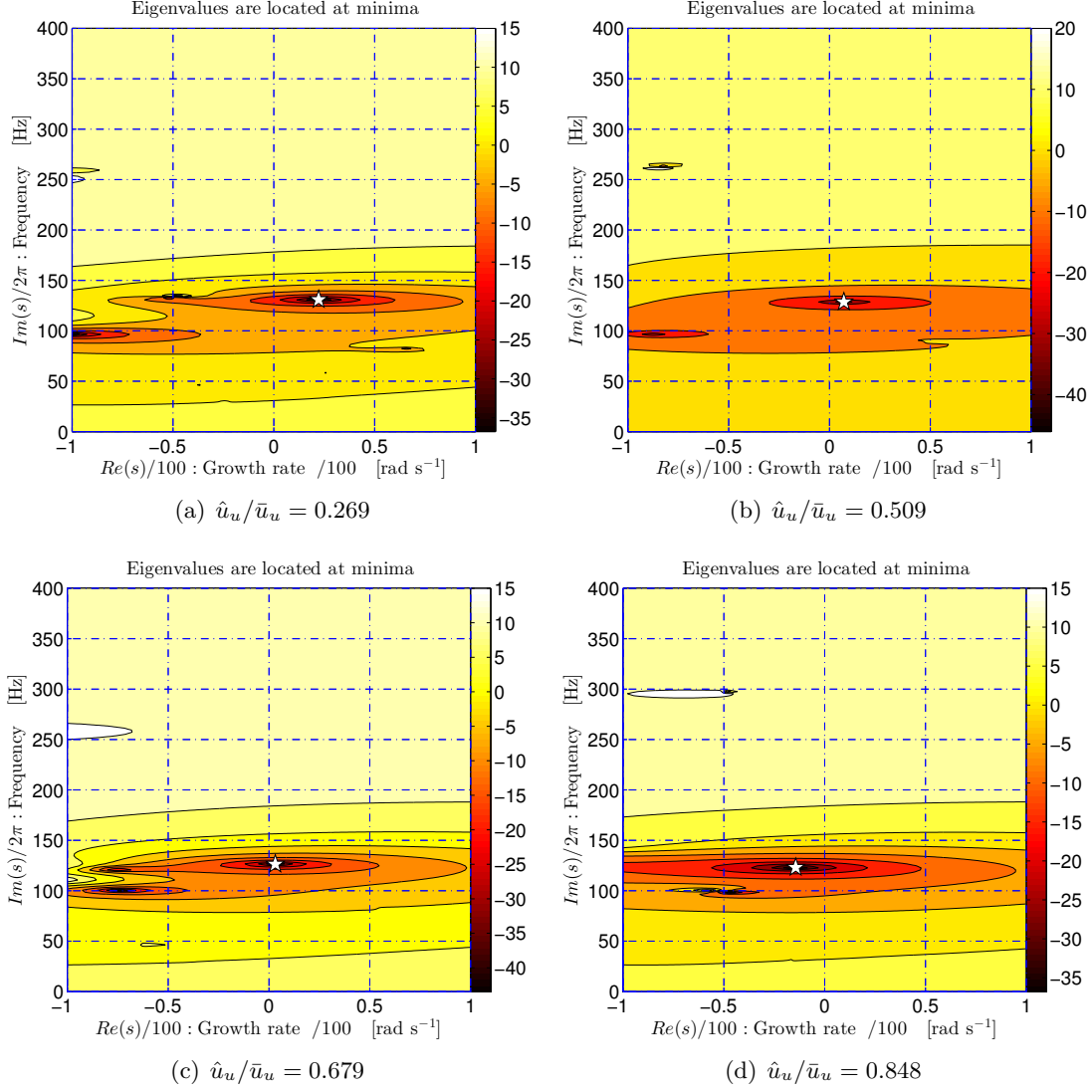
Figure 10: Contour map of $20\log_{10}|\delta e(s)|$ in the s-plane for different normalized velocity perturbations. The main modes of the system are indicated by the white stars.
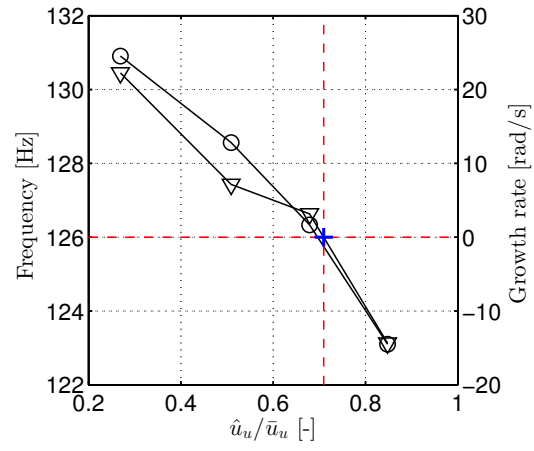
Figure 11: Evolution of the eigenfrequency (marked ○) and corresponding growth rate (marked ▽) with normalized velocity perturbations $\hat{u}_u/\bar{u}_u$. The blue marker + represents the predicted normalized velocity perturbation when the limit cycle is established.

5   Time domain simulation approach

One now progresses to the time domain simulation approach. A commonly used method for analysing nonlinear thermoacoustic instabilities in the time domain is the Galerkin discretization, which involves expanding the pressure perturbation as a Galerkin series [38, 39, 40]. The partial differential thermoacoustic wave equation is then reduced to a set of ordinary differential equations with coefficients dependent on the nonlinear acoustic loss or heat sources [41, 42, 43]. However, this approach is based on a continuous spatial approximation [44] and is limited to simple combustor configurations, although recent efforts have accounted for the temperature jump across the flame [45, 46]. Other discretization methods such as the modal expansion technique, have been used to produce a state-space representation for time domain simulations [47]. The wave-based approach is the one used in the present work. It has the benefits of extending easily to combustion chambers with varying cross sectional area and annular geometries and can account for a wide range of acoustic boundary conditions [6, 48]. It can also account for discontinuous acoustic velocity and temperature distributions using jump equations [49, 50] (or see Eq. 23).

Time domain simulations are based on the inverse Laplace transform of the governing frequency domain equations. The three wave strengths are sampled with equal sample time T for conversion to the time domain.

$$A_k^+(nT) = A_k^+[n] \tag{59a}$$

$$A_k^-(nT) = A_k^-[n] \tag{59b}$$

$$E_k^+(nT) = E_k^+[n] \tag{59c}$$

where $n = 1, 2, \cdots N$. The exponential terms $\exp(-\tau s)$ are transformed to time delays τ. Linear interpolation is used to calculate a signal $s(t)$ delayed with τ, which can be mathematically expressed as:

$$s(t - \tau) = s[n_\tau] + (s[n_\tau + 1] - s[n_\tau])\Big(\frac{\tau}{T} - n_\tau\Big) \tag{60}$$

where $n_\tau = \lfloor \tau/T \rfloor$. The function $\lfloor \cdot \rfloor$ returns the nearest integer smaller than the input value. The treatments of the relations at the boundaries and interfaces between different modules are detailed in following sections.

5.1 Jump equations at interfaces without heat perturbation

At interfaces without heat perturbations (the interface is for example described by k), the time domain relation between the thermal properties either side can be expressed as:

$$\mathcal{B}_{k,2}\mathcal{C}_2 \begin{bmatrix} A_{k+1}^+(t) \\ A_{k+1}^-(t - \tau_{k+1}^-) \\ E_{k+1}(t) \end{bmatrix} = \mathcal{B}_{k,1}\mathcal{C}_1 \begin{bmatrix} A_k^+(t - \tau_k^+) \\ A_k^-(t) \\ E_k(t - \tau_k^s) \end{bmatrix} \tag{61}$$

where, as mentioned in the previous sections, $\mathcal{B}_{k,1}$, $\mathcal{B}_{k,2}$, $\mathcal{C}_1$ and $\mathcal{C}_2$ are constant matrices. The exponential terms are transformed to time delays. The incident waves $A_k^+(t - \tau_k^+)$, $A_{k+1}^-(t - \tau_{k+1}^-)$ and $E_k(t - \tau_k^s)$ are known at time step t, and are hence used to calculate the emitted waves $A_{k+1}^+(t)$, $A_k^-(t)$ and $E_{k+1}(t)$ from the interface.

5.2 Jump equations at interfaces with heat perturbations

The link becomes more complicated in the presence of a flame or an unsteady heat source, as shown in equation 62.

$$\mathcal{B}_{k,2}^{\text{ii}}\mathcal{C}_2 \begin{bmatrix} A_{k+1}^+(t) \\ A_{k+1}^-(t - \tau_{k+1}^-) \\ E_{k+1}(t) \end{bmatrix} = \mathcal{B}_{k,1a}^{\text{ii}}\left(\mathcal{B}_{k,2}^{\text{i}}\right)^{-1}\mathcal{B}_{k,1}^{\text{i}}\mathcal{C}_1 \begin{bmatrix} A_k^+(t - \tau_k^+) \\ A_k^-(t) \\ E_k(t - \tau_k^s) \end{bmatrix}$$

$$+ \begin{bmatrix} 0 \\ 0 \\ \dfrac{\Delta H}{\Theta_k \bar{c}_k \bar{c}_{k+\frac{1}{2}}} \end{bmatrix} G(\hat{u}_k(t - \tau_f)/\bar{u}_k, t) * \left(A_k^+(t - \tau_k^+) - A_k^-(t)\right) \tag{62}$$

The heat release rate perturbation $\dot{q}'$ is calculated in the second component on the right side of the equation, by the convolution operation (represented as the symbol $*$) of the flame describing function $G(\hat{u}_k/\bar{u}_k, t)$ and velocity perturbations $u_k'(t) = \left(A_k^+(t - \tau_k^+) - A_k^-(t)\right)/\bar{\rho}_k\bar{c}_k$. To use flame describing functions in the time domain simulations, they are convected into Green's functions by taking the inverse Laplace transform (or inverse Fourier transform for causal systems [48]). Furthermore, the flame describing function also depends on the normalized velocity perturbation amplitude $\hat{u}_k(t - \tau_f)/\bar{u}_k$ at the time step

$t - \tau_f$, where τ_f indicates the time for disturbances to be convected from the base to the tip for premixed flames [14] and is, for example, directly used in the $n - \tau$ model [9] as the time lag of heat release rate perturbations with respect to oncoming flow perturbations. In time domain simulations, it is necessary to update the flame describing function and its Green's function every time step based on the latest value of $\hat{u}_k(t - \tau_f)/\bar{u}_k$. The difficulty now is to calculate the signal envelope $\hat{u}_k$.

5.2.1 Calculation of signal envelope based on root mean square value (RMS)

For velocity perturbations with weak growth rate or attenuation rate, the value $\hat{u}$ can be evaluated by the RMS value within a time period. The calculation method is for example proposed by Li and Morgans [51] and can be briefly described as following. Velocity perturbations with weak growth rate or attenuation rate, can be expressed as the summation of different modes with the growth rate σ_k and angular frequency $\omega_k = 2\pi f_k$ respectively:

$$u'(t) = \text{real}\left(\sum_{k=1}^{n} \mathcal{B}_k \exp\left(\sigma_k + i\left(\omega_k t + \theta_k\right)\right)\right) \tag{63}$$

where $\mathcal{B}_k$ is the amplitude of kth mode and θ_k denotes the phase. The value $\left(\sum_{k=1}^{n} \mathcal{B}_k^2 \right)^{1/2}$ is used to measure the amplitude $\hat{u}$ of the combined signal $u'(t)$. The eigenfrequency of the kth mode can be approximately expressed as $f_k = k f_1$ in the Rijke tube [52]. Denoting the period of the first mode as $\tau = 1/f_1$, one can obtain the RMS value along the time interval $[t - \tau/2, t + \tau/2]$:

$$RMS\left(u'(t)\right)\Big|_{t-\frac{\tau}{2}}^{t+\frac{\tau}{2}} = \left(\frac{1}{\tau} \int_{-\frac{\tau}{2}}^{\frac{\tau}{2}} \left(u'(t)\right)^2 \mathrm{d}t \right)^{1/2}$$

$$= \left(\frac{1}{\tau} \int_{-\frac{\tau}{2}}^{\frac{\tau}{2}} \left(\sum_{k=1}^{n} \mathcal{B}_k^2 \exp\left(2\sigma_k t\right) \cos^2\left(\omega_k t + \theta_k\right) + \sum_{k\neq i} \mathcal{B}_k \mathcal{B}_i \exp\left((\sigma_k + \sigma_i)t\right) \cos\left(\omega_k t + \theta_k\right) \cos\left(\omega_i t + \theta_i\right) \right) \mathrm{d}t \right)^{1/2} \tag{64}$$

Assuming $\sigma_k \tau \to 0$, the above equation can be simplified as:

$$RMS\left(u'(t)\right)\Big|_{t-\frac{\tau}{2}}^{t+\frac{\tau}{2}} \approx \left(\frac{1}{2} \sum_{k=1}^{n} \mathcal{B}_k^2 \right)^{1/2} = \frac{\sqrt{2}}{2}\hat{u} \tag{65}$$

The RMS value was also experimentally used in [53, 22] to analyze multi-mode combustion instabilities. We thus use $\sqrt{2}RMS$ to measure the amplitude of $u'(t)$, and take $\tau = 1/f_1$.

31

5.2.2 Calculation of signal envelope based on Hilbert transform

Combustion instabilities typically onset rapidly and disturbances grow to a limit cycle in a very short time period for most industrial combustors [5]. Furthermore, when a control approach is implemented to suppress the instabilities, the disturbances may be attenuated very quickly [54]. The previous method is then not suitable and the Hilbert transform [55] is used as an alternative to calculate the signal envelope amplitude when the magnitudes of harmonics are relatively weak compared to the fundamental frequency term in the Fourier series of the envisaged signal [56, 57]. To determine the envelope of a signal, its analytical signal is constructed by the following procedure [58, 59]. For any real valued signal $s(t)$, one associates a complex valued signal $s_a(t)$ defined as:

$$s_a(t) = s(t) + i\mathscr{H}(s(t)) \tag{66}$$

where $\mathscr{H}(s(t))$ is the Hilbert transform of $s(t)$, and is the time domain convolution of $s(t)$ with the function $1/(\pi t)$ [55]. The original real signal $s(t)$ is simply the real part of this analytical representation. This imaginary component $\mathscr{H}(s(t))$ corresponds to signal which is rotated by 90° in the complex plane with the same magnitude and frequency content as the real signal. The envelope can be evaluated by the absolute value of the analytical form of a narrow-band signal $s(t)$:

$$\hat{s}(t) = |s_a(t)| \tag{67}$$

Furthermore, the Fourier transform of the analytical signal $\tilde{s}_a(f)$ is a one-side spectrum. Only the positive frequency band is presented and is equal to twice the Fourier transform of the real signal $\tilde{s}_a(f) = 2\tilde{s}(f)$ for $f > 0$. This property enables the use of the Fourier transform and inverse Fourier transform to evaluate the Hilbert transform, which is used in the Matlab command "*hilbert*". We herein only consider discrete signals in the time domain simulations. The procedure can be briefly described as following:

- We assume that a continuous real signal $s(t)$ with a finite length is equally sampled $s(nT) = s[n]$, $n = 1, 2, \cdots N$ at periodic time intervals of T seconds, where T is carefully chosen to avoid aliasing. The spectrum of the real discrete signal is obtained from a discrete Fourier transform (DFT), which is complex symmetric:

$$\tilde{s}[k] = \sum_{n=1}^{N} s[n] \exp\big(-i2\pi f[k](n-1)T\big) \qquad k = 1, 2, \cdots N \tag{68}$$

  where, the discrete frequency sample equals to $f[k] = (k-1)/(NT)$.

- A frequency domain filter proposed by Marple [60] is then used to create a one-sided spectrum. The discrete filter can be mathematically expressed as:

$$\mathscr{O}[k] = \begin{cases} 1 & \text{for } k = 1 \text{ and } k = \frac{N}{2} + 1 \text{ if } N \text{ is even.} \\ 2 & \text{for } 2 \le k \le \lceil \frac{N}{2} \rceil. \\ 0 & \text{else.} \end{cases}$$

where, the symbol $\lceil \cdot \rceil$ denotes the ceiling function returning the nearest integer greater than the input value.

- A discrete-time complex signal $s_{a,p}[n]$ with the same length as the real signal $s[n]$ is obtained as an estimation of the analytical signal $s_a[n]$, using an inverse discrete Fourier transform (IDFT) of the frequency domain filtered signal $\mathscr{O}[k]\tilde{s}[k]$, which writes:

$$s_{a,p}[n] = \frac{1}{N} \sum_{k=1}^{N} \mathscr{O}[k]\tilde{s}[k] \exp\left(\frac{i2\pi(k-1)(n-1)}{N}\right) \qquad n = 1, 2, \cdots N \qquad (69)$$

The envelope signal $\hat{s}$ is predicted by calculating the absolute value of the complex signal $s_{a,p}$. Since the DFT and IDFT are used in evaluating the envelope of a real discrete signal $s[n]$, to improve the processing resolution, one has to use a large time sample length, which comprises the knowledge before and after the time step nT. This may consequently increase the memory for calculation and require the knowledge that has not been calculated yet. Now it is necessary to investigate the length of samples on the prediction precision. This may be explained more clearly using the example shown in figure 12. The input signal oscillates with a pure frequency of $f = 117$ Hz and a growth rate of $\sigma = 27$ s^{-1}. The envelope of the signal equals to $\hat{s}(t) = e^{27t}$. This example is similar to those instabilities growing within an unstable combustor. In the time domain simulations, this signal is sampled with time step $T = 10^{-4}$ s, which is sufficiently small to avoid aliasing. Fig. 12(a) shows the signal and its predicted envelopes. To predict the envelope in the interval [0.04 0.06] s, the Hilbert transform method is carried out with different sample lengths. Figure 12(b) shows the precision $\left| |s_a[n]| - |s_{a,p}[n]| \right| / |s_a[n]|$ with time. The precision is improved using longer sample length and the ringing effect is reduced by zero padding. This method is used in time domain simulations of OSCILOS if knowledge of the signal envelope is desired.

As mentioned above, the estimation of signal envelope also needs the knowledge of "future" time steps. A "guess-and-comparison" method is used, which is summarized using the flow chart presented in figure 13.

(a) Raw signal and its predicted envelope.
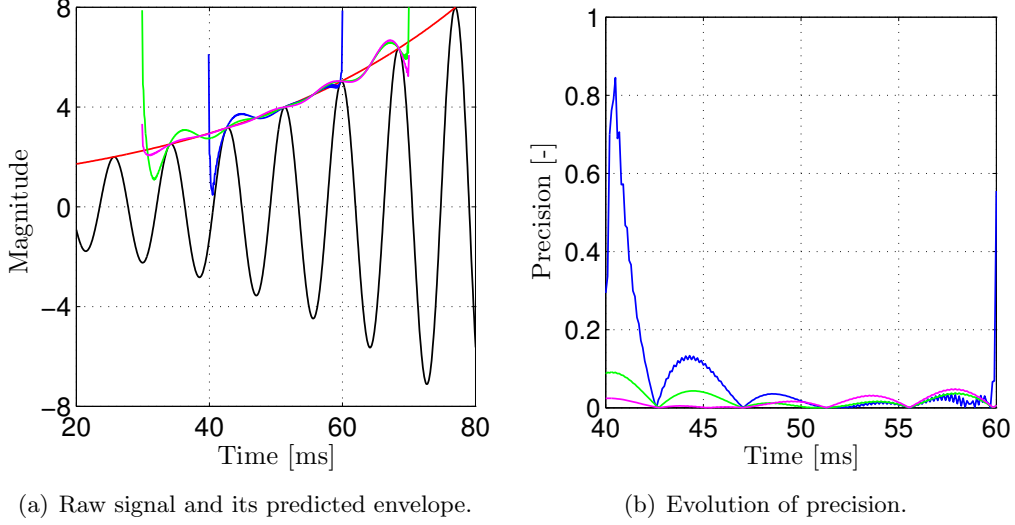
(b) Evolution of precision.

Figure 12: Comparisions between predicted envelope of a growing oscillating signal $s(t)$ based on different time sample lengths and end corrections. ——: signal $s(t) = e^{\sigma t}\cos(2\pi f t)$, where the frequency f equals to 117 Hz and the growth rate σ equals to 27 s^{-1}; ——: signal envelope $\hat{s}(t) = e^{\sigma t}$; ——: predicted envelope $\hat{s}_{p1}(t)$ from the samples within time interval [0.04 0.06] s; ——: predicted envelope $\hat{s}_{p2}(t)$ from the samples in time interval [0.03 0.07] s; ——: predicted envelope $\hat{s}_{p3}(t)$ from the samples in time interval [0.03 0.07] s. The beginning and the end of the signal are padded by zeros with the length of one quarter of the raw signal to reduce the ringing effect.

5.3   Boundary conditions

Time domain simulations are carried out from the inlet to the outlet. The entropy waves are considered to undergo shear dispersion when they are convected with the mean flow such that they are fully attenuated when they reach the end of the combustor. The incident pressure wave at the combustor end thus is the only source of the reflected waves. If the reflection coefficients have constant values, the reflected waves from the boundaries follow easily as:

$$A_1^+[n] = R_1 A_1^-(t - \tau_1^-) \tag{70a}$$

$$A_N^-[n] = R_2 A_N^+(t - \tau_N^+) \tag{70b}$$

If the reflection coefficient is expressed in transfer function form, it is converted into a Green's function for time domain simulations using the same method as for the flame describing function. The reflected waves are calculated by the convolution operation of
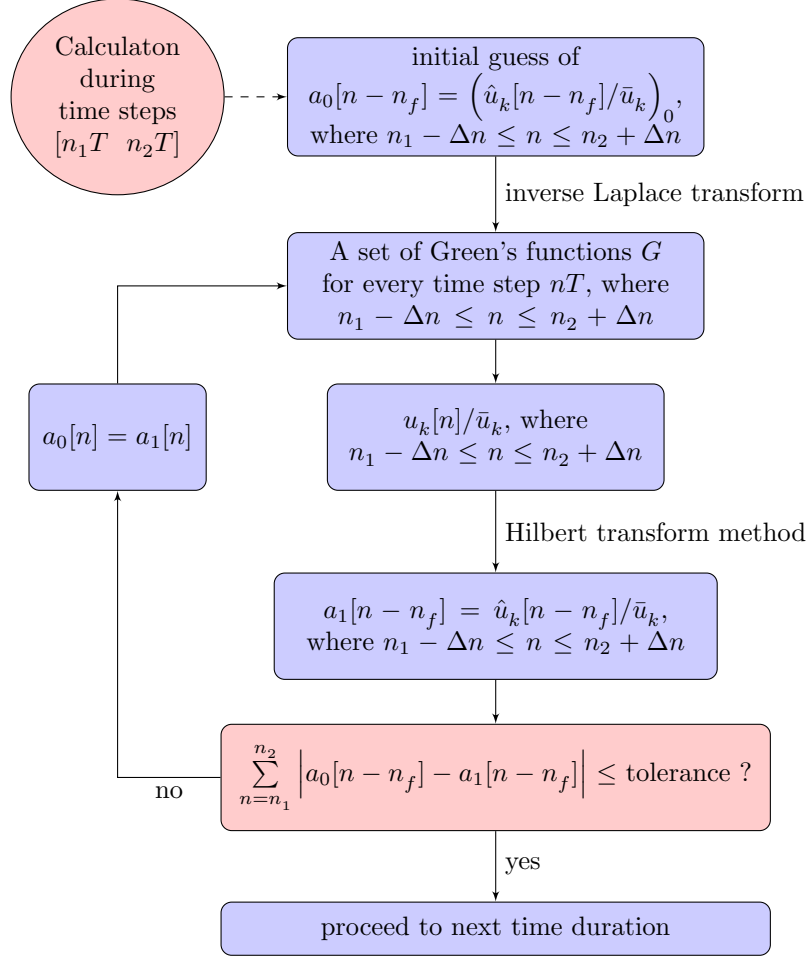
34

Figure 13: Flow chart of the "guess-and-comparison" method. Prediction of signal envelope in the time duration $[n_1 T \quad n_2 T]$ is carried out using the knowledge with a larger sample length $n_1 - \Delta n \leq n \leq n_2 + \Delta n$, where Δn denotes the number of additional samples padded at the two ends of raw signal.

the pressure reflection transfer function and incident waves:

$$A_1^+[n] = R_1(t) * A_1^-(t - \tau_1^-) \tag{71a}$$

$$A_N^-[n] = R_2(t) * A_N^+(t - \tau_N^+) \tag{71b}$$
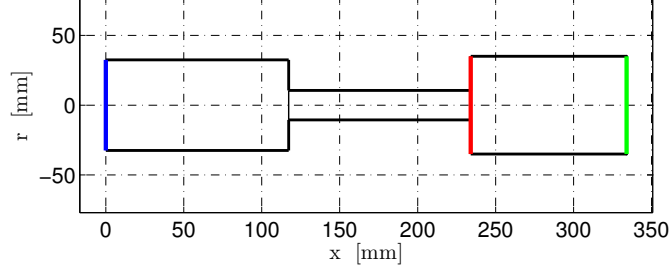
Figure 14: Combustor shape. The inlet and outlet are represented by the blue and green lines, respectively. The flame is considered as "compact" and is indicated by the red line.

5.4   Validation and test cases

Validation of the time domain simulation code is carried out using a stable combustor, which is presented in the following. Unstable cases in which the flame describing functions were used can be viewed in our recent papers [25, 51].

5.4.1   Case 1: stable combustor

We first consider a stable case. The experiments were still carried out by Palies and co-workers in Laboratory EM2C [36]. The length of combustor is selected such that the system is stable. In the simulations, the combustor is simplified to three cylinders. The lengths of the three modules are 117.3 mm, 117 mm and 100 mm respectively; corresponding radii are 32.5 mm, 10.585 mm and 35 mm respectively. The combustor shape is shown in figure 14. The flame is considered "compact". The mean velocity at the outlet of the injection unit is $\bar{u}_2 = 4.13$ m/s. The mean pressure is $\bar{p}_1 = 1$ bar and the mean temperature is $\overline{T}_1 = 300$ K. The temperature of the burned gases is $\overline{T}_3 = 1600$ K. As shown in previous tests, OSCILOS predicts the eigenfrequency and growth rate of stable and unstable combustor well. The objective of this test case is to show that these phenomena can also be reproduced in the time domain simulations. To simplify the simulations, a simple linear flame model is used, which can be mathematically expressed as:

$$\widetilde{T}(s) = \frac{\omega_c^2}{s^2 + 2\xi\omega_c s + \omega_c^2} e^{-\tau_f s} \tag{72}$$

where $\omega_c = 2\pi f_c$ denotes the angular cut-off frequency and $f_c = 200$ Hz. $\xi = 0.5$ is the damping ratio of the second order low-pass filter model. $\tau_f = 2$ ms. The Green's function of the transfer function in the time domain is shown in Fig. 15. The absolute value of

36

the Green's function decreases with time and converges to negligible values when $t = 11$ ms. The convergence time is sufficiently small to enable reduction computing time. The inlet boundary is considered as a rigid wall with pressure reflection coefficient $R_1 = 1$. The outlet is open to atmosphere with reflection coefficient a constant $R_2 = -1$. It is
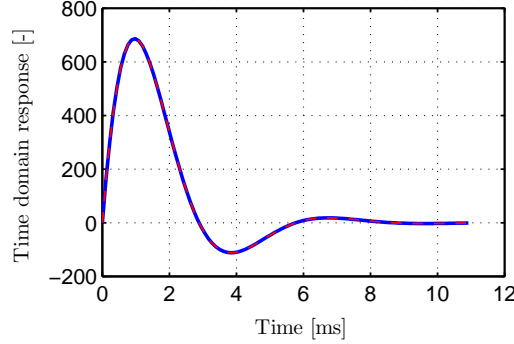

Figure 15: Time evolution of the Green's function of the flame transfer function.

then possible to analyse the stability of the system in the frequency domain. Figure 16 shows the contour map of the eigenvalues and their distributions in the s-plane. The main mode of the system is on the left side of the s-plane indicating that the system is stable. The eigenfrequency and its growth rate of this mode equal to 152.6 Hz and -19.1 s^{-1}, respectively. It is possible to stimulate the system using a loudspeaker at the end of the combustion chamber. The response of the combustor can be measured using a microphone located at the inlet of the plenum. The loudspeaker is driven by a pure sinusoidal signal with a frequency of f_p. The pressure wave from the loudspeaker is mathematically expressed as:

$$p_L = A_L \sin(2\pi f_p t) \tag{73}$$

Figure 17 shows time domain simulation results for loudspeaker signals with the amplitude of $A_L = 0.01$ Pa and different frequencies of 100 Hz, 150 Hz and 200 Hz, respectively. The response of the combustor alters with the frequency of the loudspeaker signal. When the driving frequency approaches the resonant frequency of the combustor, 152.6 Hz, the amplitude of the pressure perturbations measured by the microphone p_M increases and reaches the maximum value when the driving frequency f_p equals to the resonant frequency. This is validated by plotting the response of combustor $p_{M,rms}$ with the driving frequency, as shown in figure 18, where $p_{M,rms}$ denotes the average RMS value of the pressure signal p_M. These results match quite well the experimental results as shown in Refs. [61, 36]. OSCILOS can thus reproduce different phenomena within a combustor in the time domain.
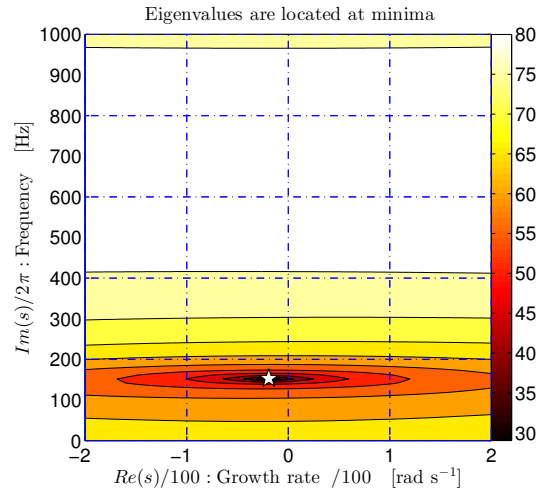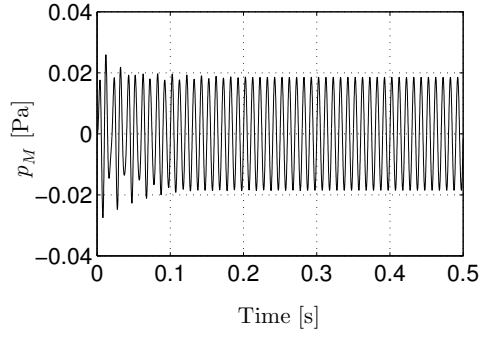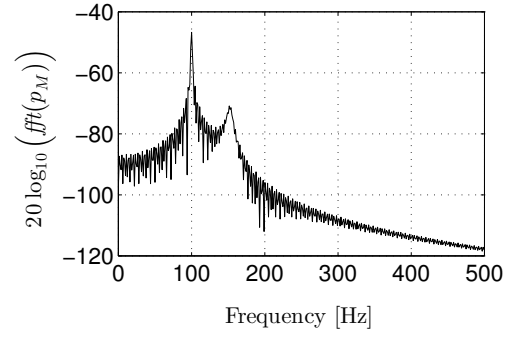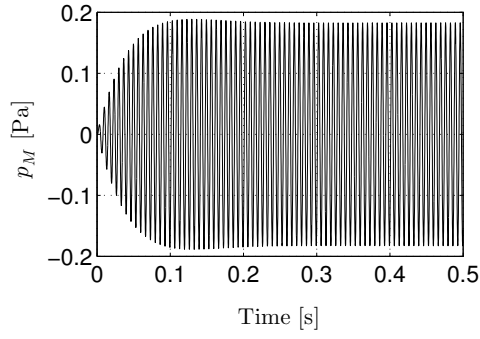
37

Figure 16: Contour map of $20 \log_{10} |\delta e(s)|$ in the s-plane. The main mode of the system is is indicated by the white star.
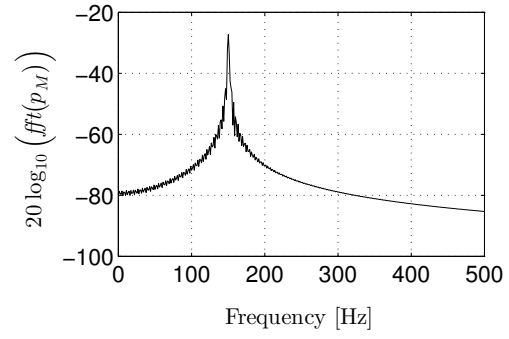
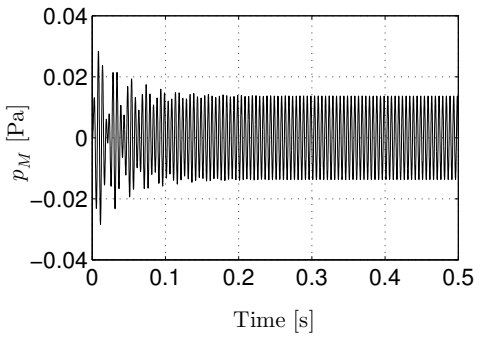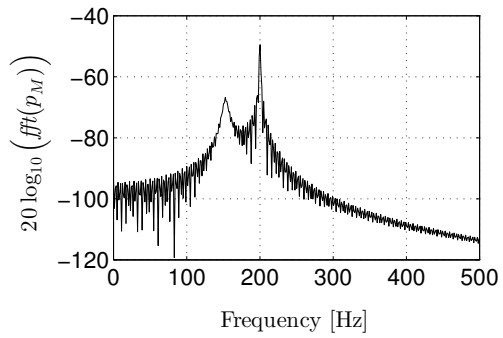(a) Time evolution. $f_p = 100$ Hz.

(b) Spectrum.

(c) Time evolution. $f_p = 150$ Hz.

(d) Spectrum.

(e) Time evolution. $f_p = 200$ Hz.

(f) Spectrum.

Figure 17: Time evolutions of the pressure signal p_M and its fast Fourier transform (spectrum).
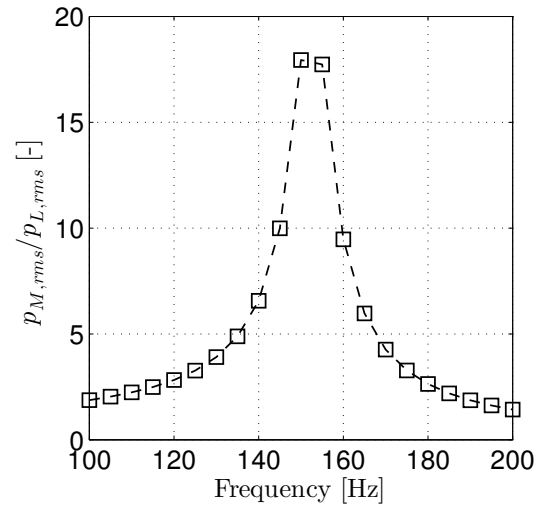
39

Figure 18: Response of the combustor loudspeaker forcing frequency at constant amplitude.

6 Passive dampers

6.1 Helmholtz Resonators (HRs)

6.1.1 Introduction to nonlinear and linear models

Helmholtz resonators are widely used as passive dampers for their simple structure and their robust acoustic absorption performance [62]. As shown in Fig. 19, a typical Helmholtz resonator consists of a small neck opening to a volume or chamber. Small pressure perturbations at the neck mouth give rise to large mass flux oscillations in the neck at resonance. This resonant frequency can be predicted by the well-known equation (which does not account for acoustic damping) $f_{\mathrm{res}} = c/(2\pi)\sqrt{S/(Vl)}$, where c is sound velocity in the chamber, S, l, V are neck cross-sectional area, neck length, and chamber volume respectively. We now present nonlinear and linear models which account for the acoustic damping of the resonator: these apply in the case of no bias flow and with bias flow (see Fig. 19(a), 19(b)) respectively.

In the absence of a neck mean flow, as shown in Fig. 19(a), energy absorption is usually related to the nonlinear viscous damping of the flow in the neck region. This can be modelled by a nonlinear model such as proposed by Cummings [63],

$$\widetilde{p}_v - \widetilde{p}_{x_h} = \alpha\bar{\rho}_n \cdot |\widetilde{u}_n| \cdot \widetilde{u}_n + i\omega\bar{\rho}_n l_{\mathrm{eff}} \cdot \widetilde{u}_n, \tag{74}$$

where $\widetilde{p}_{x_h}$ and $\widetilde{p}_v$ are the oscillating pressure amplitudes at the neck mouth and in the cavity respectively, $\widetilde{u}_n$ is the oscillating velocity amplitude in the neck defined as positive for outward flow from the cavity, l_{eff} is the effective neck length and α is the coefficient describing the nonlinear behaviour of the resonator. l_{eff} and α are both assumed to be independent of frequency [64]. $\bar{\rho}_n$ denotes air density in the neck and ω denotes angular frequency of the oscillation. This model has been successfully validated and used by many researchers such as Bellucci et al. [65], Dupère et al. [64, 66], and Zhao et al. [67].

In the presence of a mean neck flow (also called a bias flow), as shown in Fig. 19(b), incident acoustic waves cause unsteady vortices to be shed at the edges of the apertures, which are swept away by the mean flow. The local absorption is characterized by the Rayleigh conductivity [68] defined as

$$K_R = \frac{i\omega\bar{\rho}_n S_n\widetilde{u}_n}{\widetilde{p}_v - \widetilde{p}_{x_h}}, \tag{75}$$

where S_n is cross-sectional area of the neck. According to Howe et al. [68], $K_R = 2r_n(\gamma + i\delta)$, which is adapted here to the convention of positive exponent in the harmonic factor $e^{i\omega t}$.

$$\gamma + i\delta = 1 + \frac{(\pi/2)I_1(St)e^{-St} - iK_1(St)\sinh(St)}{St[(\pi/2)I_1(St)e^{-St} + iK_1(St)\cosh(St)]}, \tag{76}$$

41

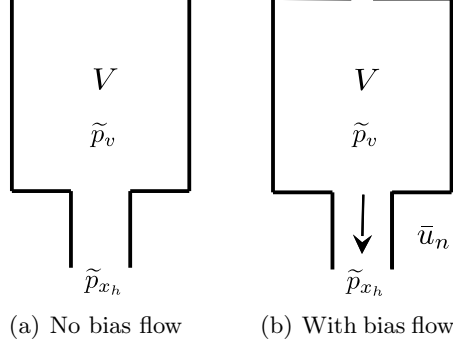<div align="center">(a) No bias flow   (b) With bias flow</div>

Figure 19: Typical Helmholtz resonators without (a) and with (b) neck mean flow.

where I_1 and K_1 are modified Bessel functions of the first and second kinds, $St = \omega \cdot r_n / \bar{u}_c$ is the neck Strouhal number, $r_n = (S_n/\pi)^{1/2}$ is the neck radius and $\bar{u}_c$ is the vortex convection velocity, which is taken to be approximately equal to the mean flow velocity in the neck by Howe [68], Hughes et al. [69], and Eldredge et al. [70]. Good experimental validation for this Rayleigh conductivity approximation has been achieved and is used in the following linear Helmholtz resonator model which applies in the presence of a mean bias flow.

The pressure difference across the neck can be approximately treated as the sum of the contributions from vortex shedding and acceleration of the fluid in the neck, leading to the following revision for the total Rayleigh conductivity [71, 70, 72, 73]:

$$\frac{1}{K_R'} = \frac{1}{K_R} + \frac{l}{S_n}, \tag{77}$$

where l is the actual length of the neck.

The size of the resonator cavity is generally assumed to be much larger than its neck size, and the cavity length to be much shorter than the acoustic wavelength. Assuming isentropic condition in the cavity, the relation between the pressure oscillations in the cavity and velocity oscillation in the neck can be written as

$$\widetilde{p}_v = -\bar{c}_v^2 \frac{\bar{\rho}_n S_n}{i\omega V} \cdot \widetilde{u}_n, \tag{78}$$

where $\bar{c}_v$ denotes the speed of sound in the cavity.

With a Helmholtz resonator attached to an acoustic module, as shown in Fig. 20, the mean flow in the duct acts as a grazing flow at the resonator neck mouth, and affects the sound absorption performance of the resonator [74, 64]. As the mean flow velocity in combustors is generally small, the nonlinear model assumes that the amplitude of the
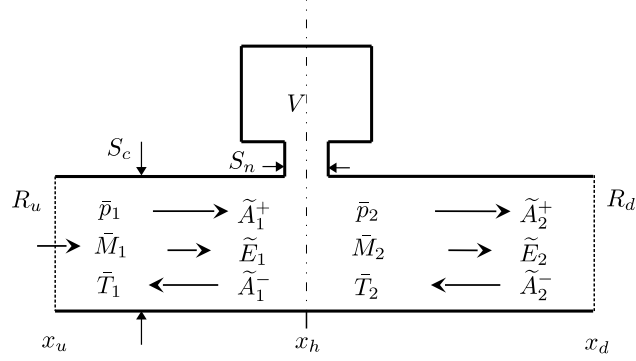
<div align="center">42</div>

Figure 20: A Helmholtz resonator installed in an acoustic duct.

oscillating velocity in the neck is large and the linear grazing flow effect can be ignored. Experimental validation of this nonlinear model with negligible and small mean flows has been performed by Dupère et al. [64, 66], and Zhao et al. [67]. For the linear model, which applies when there is a mean bias flow in the neck, the sound absorbed by the hole has been shown to be dominated by the bias flow when the bias flow speed is relatively high [75, 70]. Dupère et al. [64] showed that only a small amount of bias flow is required to destroy the sound generation by the interaction between the grazing flow and neck hole, meaning that the effect of the grazing flow is neglected in the present linear model. It is noted that in the case of a small mean bias flow and a relatively large grazing flow, the effect of the grazing flow may need to be accounted for.

6.1.2 Calculation procedures

Using the mass, momentum and energy conservation relations, the mean flow parameters before (denoted by subscript $_1$), after the resonator (denoted by subscript $_2$) and at the resonator neck (denoted by subscript $_n$) can be related by

$$\bar{m}_2 = \bar{m}_1 + \bar{m}_n, \tag{79a}$$

$$\bar{f}_2 = \bar{f}_1, \tag{79b}$$

$$\bar{e}_2 = \bar{e}_1 + \bar{e}_n. \tag{79c}$$

where $\bar{m}$, $\bar{f}$, and $\bar{e}$ denote mass, axial momentum and energy flux, respectively. The momentum in the x-direction is constant because the neck flow is assumed to be in the

radial direction of the main duct. Equations (79) can be written as

$$\bar{\rho}_2 \bar{u}_2 = \bar{\rho}_1 \bar{u}_1 + \bar{\rho}_n \bar{u}_n \frac{S_n}{S_c}, \tag{80a}$$

$$\bar{p}_2 + \bar{\rho}_2 \bar{u}_2^2 = \bar{p}_1 + \bar{\rho}_1 \bar{u}_1^2, \tag{80b}$$

$$\bar{\rho}_2 \bar{u}_2 (C_{p2}\bar{T}_2 + 0.5\bar{u}_2^2) = \bar{\rho}_1 \bar{u}_1 (C_{p1}\bar{T}_1 + 0.5\bar{u}_2^2) + \bar{\rho}_n \bar{u}_n \frac{S_n}{S_c}(C_{pn}\bar{T}_n + 0.5\bar{u}_n^2), \tag{80c}$$

where $C_{p(1,2,n)}$ denotes heat capacity at constant pressure, which is a function of the temperature and the ideal gas relation gives $\bar{p}_{1,2} = \bar{\rho}_{1,2}R\bar{T}_{1,2}$. The mean temperature in the cavity, $\bar{T}_v$ (and thus $\bar{c}_v$), is given by the user when setting up the Helmholtz resonator model. The mean neck temperature and density are assumed to match those in the cavity. The effect of hot-gas penetration and high amplitude oscillations in the neck of the resonator has been shown to slightly alter both the resonant frequency and sound absorption coefficient of the Helmholtz resonator [76, 77], depending on the temperature difference between the cavity and the duct, the bias flow velocity in the neck and the pressure oscillation amplitude at the entrance of the resonator. Generally, the neck temperature and density match those in the cavity for the linear model in which the mean bias flow is assumed to dominate the flow in the neck. In the absence of neck bias flow, when the non-linear model is used, the neck temperature and density match those in the cavity for half an oscillation period but then tend to increase due to heat intrusion from the acoustic duct during the other half. More accurate models incorporating neck temperature variations may therefore be incorporated into later versions of this simulator.

$\bar{\rho}_2$, $\bar{u}_2$ and $\bar{T}_2$ can be calculated from Eqs. (80). In practice, as the mean volume flux from the resonator is generally very small ($S_n/S_c \ll 1$), the mean duct flow parameters are generally found to be similar to those before the resonator.

The mass, momentum and energy conservation equations can then be considered for fluctuations, retaining only linear contributions to give

$$\widetilde{m}_2 = \widetilde{m}_1 + \widetilde{m}_n, \tag{81a}$$

$$\widetilde{f}_2 = \widetilde{f}_1, \tag{81b}$$

$$\widetilde{e}_2 = \widetilde{e}_1 + \widetilde{e}_n. \tag{81c}$$

where $\widetilde{e}_n = \bar{B}_n \widetilde{m}_n + \bar{m}_n \widetilde{B}_n$ denotes the energy flux oscillation from the resonator into the main duct. $\bar{B}_n = C_{pn}\bar{T}_n + 0.5\bar{u}_n^2$ is the mean neck stagnation enthalpy, with $\widetilde{B}_n$ the oscillation of stagnation enthalpy in the neck which is approximately equal to that in the cavity. Mass, momentum and energy flux perturbations in the main duct can be related to the downstream and upstream travelling acoustic wave strengths and entropy wave

44

strength by

$$
\begin{bmatrix} \widetilde{m}(x) \\ \widetilde{f}(x) \\ \widetilde{e}(x) \end{bmatrix} = \boldsymbol{M_{w2f}} \begin{bmatrix} \widetilde{A}^+(x) \\ \widetilde{A}^-(x) \\ \widetilde{E}(x) \end{bmatrix} , \tag{82}
$$

where the wave to flux transfer matrix is

$$
\boldsymbol{M_{w2f}} = S_c \begin{bmatrix} \frac{\bar{M}+1}{\bar{c}} & \frac{\bar{M}-1}{\bar{c}} & \frac{-\bar{M}}{\bar{c}} \\ (\bar{M}+1)^2 & (\bar{M}-1)^2 & -\bar{M}^2 \\ \bar{c}\left(\frac{\gamma\bar{M}}{\gamma-1} + \frac{\bar{M}^3}{2} + \frac{1}{\gamma-1} + \frac{3}{2}\bar{M}^2\right) & \bar{c}\left(\frac{\gamma\bar{M}}{\gamma-1} + \frac{\bar{M}^3}{2} - \frac{1}{\gamma-1} - \frac{3}{2}\bar{M}^2\right) & -\bar{c}\frac{\bar{M}^3}{2} \end{bmatrix} . \tag{83}
$$

To close the relations in Eqs. (81), resonator models to link $\widetilde{m}_n$ with pressure oscillation at the resonator mouth, $\widetilde{p}_{x_h}$ must be included. For the nonlinear Helmholtz resonator model, Eq. (74) is used while for the linear model Eqs. (75) and (77) are used. The calculations for the nonlinear and linear Helmholtz resonator models are then summarized bellow.

Nonlinear model:
Governing equations:

$$
-\widetilde{p}_{x_h} = \alpha\bar{\rho}_n \cdot |\widetilde{u}_n| \cdot \widetilde{u}_n + i\omega\bar{\rho}_n l_{\text{eff}} \cdot \widetilde{u}_n + \bar{c}_v^2 \frac{\bar{\rho}_n S_n}{i\omega V} \cdot \widetilde{u}_n, \tag{84a}
$$

$$
\boldsymbol{M^2_{w2f}} \begin{bmatrix} \widetilde{A}_2^+ \\ \widetilde{A}_2^- \\ \widetilde{E}_2 \end{bmatrix} = \boldsymbol{M^1_{w2f}} \begin{bmatrix} \widetilde{A}_1^+ \\ \widetilde{A}_1^- \\ \widetilde{E}_1 \end{bmatrix} + \begin{bmatrix} \widetilde{m}_n \\ 0 \\ \widetilde{e}_n \end{bmatrix} , \tag{84b}
$$

where $\boldsymbol{M^2_{w2f}}$ and $\boldsymbol{M^1_{w2f}}$ are wave to flux transfer matrixes immediately after and before the resonator respectively. Nonlinear Eq. (84a) is solved numerically for the acoustic velocity, $\widetilde{u}_n$, for a given neck pressure, $\widetilde{p}_{x_h} = \widetilde{A}_1^+ + \widetilde{A}_1^-$. Then $\widetilde{m}_n$ and $\widetilde{e}_n$ can be written as functions of the acoustic waves. Finally, acoustic and entropy waves before and after the nonlinear Helmholtz resonator are linked by Eq. (84b).

45

Linear model:

Governing equations:

$$\widetilde{u}_n = -\left(\widetilde{A}_1^+ + \widetilde{A}_1^-\right)/Z_{HR} \tag{85a}$$

$$\boldsymbol{M^2_{w2f}} \begin{bmatrix} \widetilde{A}_2^+ \\ \widetilde{A}_2^- \\ \widetilde{E}_2 \end{bmatrix} = \boldsymbol{M^1_{w2f}} \begin{bmatrix} \widetilde{A}_1^+ \\ \widetilde{A}_1^- \\ \widetilde{E}_1 \end{bmatrix} + \begin{bmatrix} \widetilde{m}_n \\ 0 \\ \widetilde{e}_n \end{bmatrix}, \tag{85b}$$

where $\widetilde{m}_n$ and $\widetilde{e}_n$ can be calculated from $\widetilde{u}_n$. Z_{HR} is the specific neck mouth impedance which is calculated by

$$Z_{HR} = \frac{i\omega\bar{\rho}_n S_n}{K'_R} + \bar{c}_v^2 \frac{\bar{\rho}_n S_n}{i\omega V}. \tag{86}$$

Finally, acoustic and entropy waves before and after the linear Helmholtz resonator can be linked by Eq. (85b).

6.2 Perforated liners

Perforated liners as shown in Fig. 21 are extensively used in engineering systems to damp acoustics [78, 79, 71, 80]. A typical liner consists of a perforated screen lining the engine ducts and a back rigid wall or a large cavity. To adjust the mean pressure jump across the perforated screen and hence enhance its sound absorption, a second layer is sometimes added to the outside of the first one to form a double liner [70, 81].

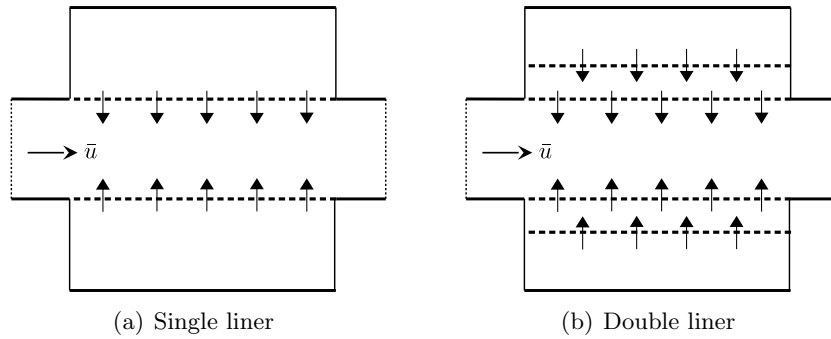(a) Single liner   (b) Double liner

Figure 21: Simplified liner configurations.

In modern combustion systems such as gas turbines and jet engines, the high temperatures present in the jet flows of these systems require that a cooling flow be blown

through a perforated liner to protect the walls of the duct enclosing the jet. This cooling flow has been found to be able to provide additional benefit of improving the effectiveness of the liner as an acoustic damper.

If the holes in the perforated liners are sufficiently separated relative to their diameters, they can be treated separately and the widely studied acoustic properties of a single orifice [68, 69, 71, 72, 73] can be used to build the liner acoustic absorption model. To investigate absorption properties of a cylindrical perforated liner in the presence of planar duct modes, Eldredge et al. [70] used an effective liner compliance based on the principle that unsteady vortex shedding from the aperture rims is the primary mechanism for absorption, and validated their results experimentally. An analytical model along these lines is developed and utilized in OSCILOS.
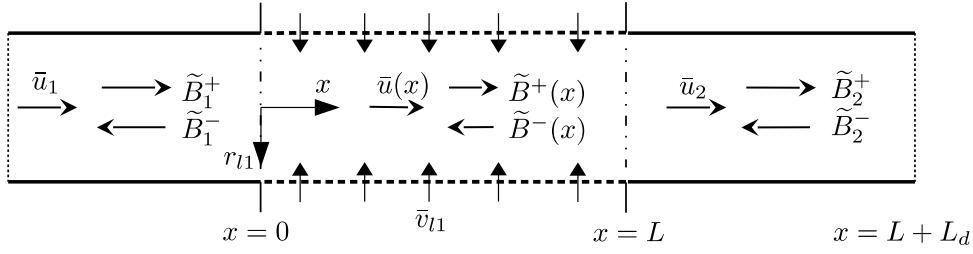

Figure 22: A perforated liner installed in an acoustic duct.

Figure 22 considers a cylindrical duct of uniform cross-section, consisting of two sections with rigid walls separated by a lined section where perforated holes are uniformly distributed. A steady flow of velocity $\bar{u}_1$, pressure $\bar{p}_1$ and temperature $\bar{T}_1$ is present in the upstream duct. A steady inward bias flow through the liner of uniform average velocity $\bar{v}_{l1}$ and temperature $\bar{T}_l$ is present in the region $x = 0 \rightarrow L$. The subscript $_{l1}$ denotes liner 1, the innermost liner. Another liner which may also be installed outside liner 1 would be denoted by a subscript $_{l2}$.

Mean temperatures in the whole liner system (in the holes of each liner, volumes between liners and the cavity outside the outermost liner) are assumed to be the same and are denoted by $\bar{T}_l$. The mean pressure and density outside the liner (or "the first liner" if a double liner system is used) are also assumed to be constant. For mean flow parameters in the main duct, the flux contribution from the mean bias flow is generally very small and causes a very slight increase of the mean duct velocity. It should be noted that temperature difference between the acoustic duct and the liner system is considered here to affect only the density of the flow, and only mass and momentum conservation equations are used to build the current liner model. A full energy conservation equation may need to be incorporated into later versions of OSCILOS when there is a large temperature difference.

6.2.1 Theoretical model – general

As shown in Fig. 22, harmonic pressure fluctuations with low frequency are considered, thus only plane waves are allowed to propagate. Because of the mean flow, the acoustic waves are described in terms of fluctuating stagnation enthalpy, $B' = p'/\bar{\rho} + \bar{u}u'$, where p' is the fluctuating pressure and u' is the fluctuating axial velocity. Then the upstream and downstream fluctuations can be written as

$$B'(x,t) = \widetilde{B}(x)e^{i\omega t} = \widetilde{B}_1^+ e^{i(\omega t + k_1^+ x)} + \widetilde{B}_1^- e^{i(\omega t + k_1^- x)}, \quad x < 0, \tag{87a}$$

$$B'(x,t) = \widetilde{B}(x)e^{i\omega t} = \widetilde{B}_2^+ e^{i(\omega t + k_2^+ x)} + \widetilde{B}_2^- e^{i(\omega t + k_2^- x)}, \quad x > L, \tag{87b}$$

$$u'(x,t) = \frac{\widetilde{B}_1^+}{(1 + \bar{M}_1)\bar{c}_0} e^{i(\omega t + k_1^+ x)} - \frac{\widetilde{B}_1^-}{(1 - \bar{M}_1)\bar{c}_0} e^{i(\omega t + k_1^- x)}, \quad x < 0, \tag{87c}$$

$$u'(x,t) = \frac{\widetilde{B}_2^+}{(1 + \bar{M}_2)\bar{c}_0} e^{i(\omega t + k_2^+ x)} - \frac{\widetilde{B}_2^-}{(1 - \bar{M}_2)\bar{c}_0} e^{i(\omega t + k_2^- x)}, \quad x > L, \tag{87d}$$

where $k_{1,2}^\pm = -\omega/\bar{c}_0/(\bar{M}_{1,2} \pm 1)$, $\bar{M}_{1,2}$ denotes mean Mach number and subscript $_{1,2}$ denote the upstream and downstream regions respectively. $\bar{c}_0 = \sqrt{\gamma R\bar{T}_1}$ is average sound speed, which is assumed to be constant in the upstream, downstream, and the lined duct sections.

$$B(x,t) = \bar{B} + \widetilde{B}(x)e^{i\omega t}, \tag{88a}$$

$$u(x,t) = \bar{u}(x) + \widetilde{u}(x)e^{i\omega t}, \tag{88b}$$

where $\bar{u}(x) = \bar{u}_1 + \bar{\rho}_l C_{l1}\bar{v}_{l1}x/\bar{\rho}_0/S_{l1}$, $C_{l1} = 2\pi r_{l1}$ is circumference of the inner wall of liner 1, $S_{l1} = \pi r_{l1}^2$ is cross sectional area of the lined duct, $\bar{\rho}_0$ is mean density in the duct (assumed to be constant in all the three duct sections), $\bar{\rho}_l$ is the mean density outside the liner and in the liner holes, and $\bar{v}_{l1}$ is the mean hole flow in liner 1.

For the flow in an infinitely small control volume in $x \in [0, \ L]$,

$$v_{l1}(x,t) = \bar{v}_{l1} + \widetilde{v}_{l1}(x)e^{i\omega t}. \tag{89}$$

Then mass conservation leads to

$$\frac{\partial \rho_0}{\partial t} + \frac{\partial(\rho_0 u)}{\partial x} = \frac{C_{l1}\rho_l}{S_{l1}}v_{l1}. \tag{90}$$

Momentum balance leads to

$$\rho_0 \frac{\partial u}{\partial t} + \rho_0 u \frac{\partial u}{\partial x} + \frac{\partial p}{\partial x} = 0. \tag{91}$$

48

Writing Eqs. (90) and (91) as the sum of mean flow and fluctuations, and subtracting the mean equations on either side, the equations in first order fluctuations can be written as

$$\frac{\partial B'}{\partial t} + 2\bar{u}(x)\frac{\partial B'}{\partial x} + \bar{c}_0^2 \frac{\partial u'}{\partial x} - \bar{u}^2(x)\frac{\partial u'}{\partial x} = \frac{C_{l1}\bar{c}_0^2 \bar{\rho}_l}{S_{l1}\bar{\rho}_0} v'_{l1}, \tag{92a}$$

$$\frac{\partial u'}{\partial t} + \frac{\partial B'}{\partial x} = 0. \tag{92b}$$

Boundary conditions for this lined region are

$$\widetilde{B}(0) = \widetilde{B}_1^+ + \widetilde{B}_1^-, \tag{93a}$$

$$\widetilde{u}(0) = \frac{\widetilde{B}_1^+}{(1 + \bar{M}_1)\bar{c}_0} - \frac{\widetilde{B}_1^-}{(1 - \bar{M}_1)\bar{c}_0}, \tag{93b}$$

$$\widetilde{B}(L) = \widetilde{B}_2^+ e^{ik_2^+ L} + \widetilde{B}_2^- e^{ik_2^- L}, \tag{93c}$$

$$\widetilde{u}(L) = \frac{\widetilde{B}_2^+ e^{ik_2^+ L}}{(1 + \bar{M}_2)\bar{c}_0} - \frac{\widetilde{B}_2^- e^{ik_2^- L}}{(1 - \bar{M}_2)\bar{c}_0}. \tag{93d}$$

To solve $\widetilde{B}^\pm(x)$ from Eqs. (92), $\widetilde{v}_{l1}(x)$ needs to be related to $\widetilde{B}^\pm(x)$. This is done by including the compliance of the first liner, η_{l1}, which implies a local relationship between $\widetilde{v}_{l1}(x)$ and the difference in stagnation enthalpy fluctuations across the liner.

$$\widetilde{v}_{l1}(x) = \frac{\eta_{l1}}{i\omega}[\widetilde{B}_{l1}(x) - \widetilde{B}(x)], \tag{94}$$

where $\eta_{l1} = K'_{l1}/d_{l1}^2$, $\widetilde{B}_{l1}$ is the fluctuating stagnation enthalpy immediately outside liner 1, and K'_{l1} is the Rayleigh conductivity of the hole in liner 1 with a thickness correction using the same method as in Eq. (77). $\widetilde{B}_{l1}$ depends on the specific configuration of the liner system. Two kinds of liner configurations (single liner and double liners) with two types of outer boundary conditions (large cavity and rigid wall) can be chosen by users in OSCILOS.

If a single liner model is chosen, users need to set the parameters and the outer boundary condition for liner 1. The parameters are the mean temperature $(\bar{T}_l)$, hole radius (a_{l1}), hole separation distance (d_{l1}), (the open area ratio of this layer can be calculated by combining a_{l1} and d_{l1}), liner thickness (t_{l1}), and mean hole Mach number $(\bar{M}_{h1})$. If the outer boundary is a large cavity, $\widetilde{B}_{l1} = 0$ is used, while if it is a rigid wall, users set the wall radius (r_w) and plane acoustic waves and zero mean axial flow $(\bar{u}_{l1}(x) = 0)$ in the annular cavity between the liner and the wall is used to solve the similar governing equations (Eqs. (92)). Any annular cavity outside the first liner is assumed to be closed at both ends in the axial direction.

If a double liner model is chosen, the first liner is surrounded by a second perforated liner of the same length. Eqs. (92) are again used between the two layers with no mean axial flow ($\bar{u}_{l1}(x) = 0$). Users set parameters for the two layers, together with the outside boundary condition for the second layer. The parameters to be set are mean temperature ($\bar{T}_l$) in the whole liner system, the hole radii (a_{l1} and a_{l2}), the hole separation distances (d_{l1} and d_{l2}), the liner thicknesses (t_{l1} and t_{l2}), the mean hole Mach number ($\bar{M}_{h1}$) of the first layer, and inner radius (r_{l2}) of the second layer.

6.2.2 Theoretical model: example of double liner surrounded by large cavities

The detailed equations for a double liner surrounded by a large cavity will be presented as an illustrative example. From Eq. (92), one-dimensional perturbations in the annular cavity between the two liners satisfy

$$\frac{\mathrm{d}\widetilde{B}_{l1}(x)}{\mathrm{d}x} = -i\omega\widetilde{u}_{l1}(x), \tag{95a}$$

$$i\omega\widetilde{B}_{l1}(x) + \bar{c}_l^2\frac{\mathrm{d}\widetilde{u}_{l1}(x)}{\mathrm{d}x} = -\frac{C_{l1}\bar{c}_l^2}{S_{l2}}\widetilde{v}_{l1}(x) + \frac{C_{l2}\bar{c}_l^2}{S_{l2}}\widetilde{v}_{l2}(x), \tag{95b}$$

$$\widetilde{u}_{l1}(0) = 0, \quad \widetilde{u}_{l1}(L) = 0, \tag{95c}$$

where S_{l2} is the cross sectional area of the cavity between the two layers, $\bar{c}_l$ is mean sound speed in the whole double liner and C_{l2} is the inner circumference of the second liner. $\widetilde{v}_{l1}(x)$ is calculated using Eq. (94), and $\widetilde{v}_{l2}(x)$ using

$$\widetilde{v}_{l2}(x) = \frac{\eta_{l2}}{i\omega}[0 - \widetilde{B}_{l1}(x)], \tag{96}$$

where $\eta_{l2} = K'_{l2}/d_{l2}^2$ and K'_{l2} is the Rayleigh conductivity of a hole in liner 2 with thickness correction from Eq. (77). The mean hole flow velocity for the second liner is obtained via the conservation of mean bias flow rate between the two liners.

$$\bar{M}_{h1}C_{l1}\sigma_{l1} = \bar{M}_{h2}C_{l2}\sigma_{l2}, \tag{97}$$

where $\bar{M}_{h1,2}$ are mean hole flow Mach numbers and $\sigma_{l1,l2}$ are open area ratios of the two liners.

Combining Eqs. (92) and (95), the fluctuation equations in the lined region can be written as

$$\begin{bmatrix} \mathrm{d}\widetilde{B}^+(x)/\mathrm{d}x \\ \mathrm{d}\widetilde{B}^-(x)/\mathrm{d}x \\ \mathrm{d}\widetilde{B}_{l1}(x)/\mathrm{d}x \\ \mathrm{d}\widetilde{u}_{l1}(x)/\mathrm{d}x \end{bmatrix} = \boldsymbol{M_T}(x) \begin{bmatrix} \widetilde{B}^+(x) \\ \widetilde{B}^+(x) \\ \widetilde{B}_{l1}(x) \\ \widetilde{u}_{l1}(x) \end{bmatrix}, \tag{98}$$

where $\boldsymbol{M_T}(x)$ is

$$\boldsymbol{M_T}(x) = \begin{bmatrix} -\left(\frac{i\omega}{\bar{c}_0+\bar{u}(x)} + \frac{C_{l1}\bar{c}_0\eta_{l1}\bar{\rho}_l}{2i\omega S_{l1}\bar{\rho}_0}\right) & -\frac{C_{l1}\bar{c}_0\eta_{l1}\bar{\rho}_l}{2i\omega S_{l1}\bar{\rho}_0} & \frac{C_{l1}\bar{c}_0\eta_{l1}\bar{\rho}_l}{2i\omega S_{l1}\bar{\rho}_0} & 0 \\ \frac{C_{l1}\bar{c}_0\eta_{l1}\bar{\rho}_l}{2i\omega S_{l1}\bar{\rho}_0} & \left(\frac{i\omega}{\bar{c}_0-\bar{u}(x)} + \frac{C_{l1}\bar{c}_0\eta_{l1}\bar{\rho}_l}{2i\omega S_{l1}\bar{\rho}_0}\right) & -\frac{C_{l1}\bar{c}_0\eta_{l1}\bar{\rho}_l}{2i\omega S_{l1}\bar{\rho}_0} & 0 \\ 0 & 0 & 0 & -i\omega \\ \frac{C_{l1}\eta_{l1}}{i\omega S_{l2}} & \frac{C_{l1}\eta_{l1}}{i\omega S_{l2}} & -\left(\frac{C_{l1}\eta_{l1}}{i\omega S_{l2}} + \frac{C_{l2}\eta_{l2}}{i\omega S_{l2}} + \frac{i\omega}{\bar{c}_l^2}\right) & 0 \end{bmatrix}.$$

To solve the ordinary differential equations (98) with the boundary conditions of Eqs. (93) and Eq. (95c), an analytical method is possible but too complicated, even if the variability of the mean duct flow is neglected. To solve this system numerically, a shooting method [82] can be used [70]. Our approach instead utilizes the matrix expressions shown in Eqs. (98) to relate fluctuating waves in the upstream and downstream regions of the lined duct, using a similar but more efficient method.

At first, the lined region is uniformly divided into N sections and the start axial location of each section is denoted by $x_i = (i-1)\mathrm{d}x$ where $i = 1, 2, ..., N$, $\mathrm{d}x = L/N$. For the frequency region $0 - 1000Hz$, $N = 50$ is found to be large enough for results to converge for a typical liner length. Then, using a fourth order Runge-Kutta method to solve the differential equations (98) in each section, the linking matrix between wave strengths at either side of each section can be obtained. Multiplying the linking matrixes for all the sections from the first to the last, the final linking matrix between oscillation amplitudes at the beginning $(x = 0)$ and end $(x = L)$ of the whole lined region can be achieved. This linking relation can be written as

$$\begin{bmatrix} \widetilde{B}^+(L) \\ \widetilde{B}^-(L) \\ \widetilde{B}_{l1}(L) \\ \widetilde{u}_{l1}(L) \end{bmatrix} = \widetilde{\boldsymbol{M_T}} \begin{bmatrix} \widetilde{B}^+(0) \\ \widetilde{B}^-(0) \\ \widetilde{B}_{l1}(0) \\ \widetilde{u}_{l1}(0) \end{bmatrix}, \tag{99}$$

where $\widetilde{\boldsymbol{M_T}}$ is the final linking matrix.

Boundary conditions in the annular cavity $(\widetilde{u}_{l1}(0) = 0, \widetilde{u}_{l1}(L) = 0)$ can then be incorporated into Eq. (99) to get

$$0 = \widetilde{\boldsymbol{M_T}}(4,1)\widetilde{B}^+(0) + \widetilde{\boldsymbol{M_T}}(4,2)\widetilde{B}^-(0) + \widetilde{\boldsymbol{M_T}}(4,3)\widetilde{B}_{l1}(0) + \widetilde{\boldsymbol{M_T}}(4,4)0, \tag{100}$$

which can then be easily reorganized to find the relation

$$\widetilde{B}_{l1}(0) = -\frac{\widetilde{\boldsymbol{M_T}}(4,1)}{\widetilde{\boldsymbol{M_T}}(4,3)}\widetilde{B}^+(0) - \frac{\widetilde{\boldsymbol{M_T}}(4,2)}{\widetilde{\boldsymbol{M_T}}(4,3)}\widetilde{B}^-(0). \tag{101}$$

51

Substituting Eq. (101) and the boundary conditions for the annular cavity ($\widetilde{u}_{l1}(0) = 0$, $\widetilde{u}_{l1}(L) = 0$) into Eq. (99) and reorganizing them, Eq. (99) becomes

$$
\begin{bmatrix} \widetilde{B}^+(L) \\ \widetilde{B}^-(L) \\ \widetilde{B}_{l1}(L) \end{bmatrix} = \widetilde{\boldsymbol{M}}'_{\boldsymbol{T}} \begin{bmatrix} \widetilde{B}^+(0) \\ \widetilde{B}^-(0) \end{bmatrix},
\tag{102}
$$

where

$$
\widetilde{\boldsymbol{M}}'_{\boldsymbol{T}} = \begin{bmatrix} \widetilde{\boldsymbol{M}}_{\boldsymbol{T}}(1,1) - \widetilde{\boldsymbol{M}}_{\boldsymbol{T}}(1,3)\widetilde{\boldsymbol{M}}_{\boldsymbol{T}}(4,1)/\widetilde{\boldsymbol{M}}_{\boldsymbol{T}}(4,3) & \widetilde{\boldsymbol{M}}_{\boldsymbol{T}}(1,2) - \widetilde{\boldsymbol{M}}_{\boldsymbol{T}}(1,3)\widetilde{\boldsymbol{M}}_{\boldsymbol{T}}(4,2)/\widetilde{\boldsymbol{M}}_{\boldsymbol{T}}(4,3) \\ \widetilde{\boldsymbol{M}}_{\boldsymbol{T}}(2,1) - \widetilde{\boldsymbol{M}}_{\boldsymbol{T}}(2,3)\widetilde{\boldsymbol{M}}_{\boldsymbol{T}}(4,1)/\widetilde{\boldsymbol{M}}_{\boldsymbol{T}}(4,3) & \widetilde{\boldsymbol{M}}_{\boldsymbol{T}}(2,2) - \widetilde{\boldsymbol{M}}_{\boldsymbol{T}}(2,3)\widetilde{\boldsymbol{M}}_{\boldsymbol{T}}(4,2)/\widetilde{\boldsymbol{M}}_{\boldsymbol{T}}(4,3) \\ \widetilde{\boldsymbol{M}}_{\boldsymbol{T}}(3,1) - \widetilde{\boldsymbol{M}}_{\boldsymbol{T}}(3,3)\widetilde{\boldsymbol{M}}_{\boldsymbol{T}}(4,1)/\widetilde{\boldsymbol{M}}_{\boldsymbol{T}}(4,3) & \widetilde{\boldsymbol{M}}_{\boldsymbol{T}}(3,2) - \widetilde{\boldsymbol{M}}_{\boldsymbol{T}}(3,3)\widetilde{\boldsymbol{M}}_{\boldsymbol{T}}(4,2)/\widetilde{\boldsymbol{M}}_{\boldsymbol{T}}(4,3) \end{bmatrix} .
\tag{103}
$$

By using the upstream and downstream boundary conditions in Eq. (93), relations between $\widetilde{B}_1^\pm$ and $\widetilde{B}_2^\pm$ can then be obtained.

6.3   Validation and example test cases

Validation of the damper models included in OSCILOS is now presented by comparing to results obtained from other low order modelling tools. Fig. 23(a) compares the power absorption coefficient of a Helmholtz resonator, defined as $\Delta = 1 - (|\widetilde{A}_1^-|^2 + |\widetilde{A}_2^+|^2)/(|\widetilde{A}_1^+|^2 + |\widetilde{A}_2^-|^2)$, where the wave strengths are shown in Fig. 20, with the numerical modelling results of Zhao et al. [67]. Excellent agreement is observed, as expected as both modelling tools use the nonliner model of Eq. (84a). Validation of the linear Helmholtz resonator model is done by comparing with Stow et al.'s results [83]. Fig. 23(b) shows the evolution of the frequency and growth rate of one mode of the system when changing the resonator position. Good agreement is achieved between our model and Stow et al.'s. Fig. 23(c) compares power absorption coefficient of a double liner defined as $\Delta = 1 - (|\widetilde{B}_1^-|^2 + |\widetilde{B}_2^+|^2)/(|\widetilde{B}_1^+|^2 + |\widetilde{B}_2^-|^2)$, where the wave strengths are shown in Fig. 22, with the numerical modelling results of Eldredge et al. [70]. Excellent agreement is observed again.

In OSCILOS, more than one damper, of more than one kind, can be included in the combustor system, whether linear or nonlinear flame models are used. If there are only linear damper models in the system, the forcing velocity amplitude before the flame is assumed in order to include the nonlinear flame model, and results for different flame forcing levels can then be predicted. If there are nonlinear dampers (with either linear or nonlinear flame models) in the system, the acoustic strength in the inlet duct is assumed and increased step by step to calculate evolutions of the eigenvalues of the whole system. In this case, an *inlet amplitude factor*, defined as $(|\widetilde{A}_1^+| + |\widetilde{A}_1^-|)/\bar{p}_1$, is used to specify the acoustic strength in the inlet duct.
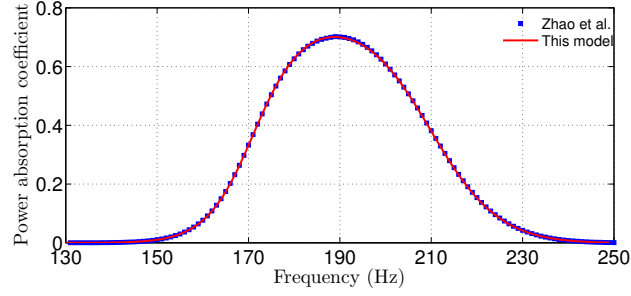
(a) Nonlinear HR model
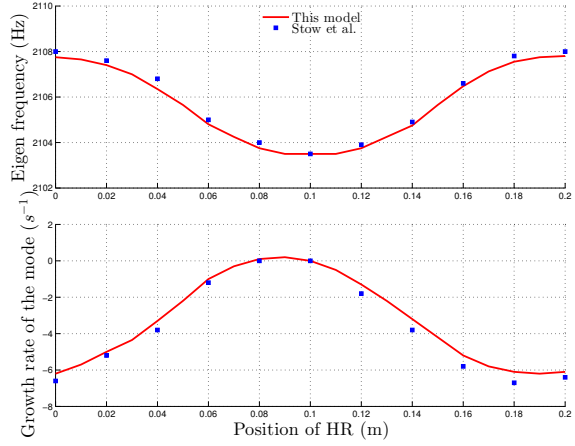
(b) Linear HR model
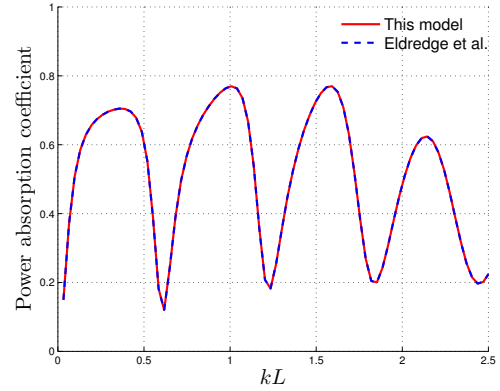
(c) Liner model

Figure 23: Validation of the damper models. (a) The nonlinear HR model is compared with results from Zhao et al. [67], (b) the linear HR model is compared with results from Stow et al. [83] and (c) the liner model is compared with results from Eldredge et al.(Figure 8) [70].

For simplicity, cases with only one damper are shown below. A simple Rijke tube is considered in Fig. 24. The radius of the tube is 50 mm, and the inlet mean flow conditions are the same for all cases: $\bar{p}_1 = 101325\ Pa$, $\bar{T}_1 = 293.15\ K$, $\bar{M}_1 = 0.001$. The mean temperature increases across the flame to give $\bar{T}_2 = 2\bar{T}_1$ and the boundary conditions are all open-open. In the cases where a linear flame model is used, an $n - \tau$ model with a 1st-order low pass filter where $a_f = 1$, $f_c = 75\ Hz$, $\tau_f = 3\ ms$ is used. The nonlinear flame model used in Case 2 is the previous linear model with a simple saturation bound, as used by Stow & Dowling [84]. The saturation bound is $\widehat{q}/\bar{q} = 0.3$.
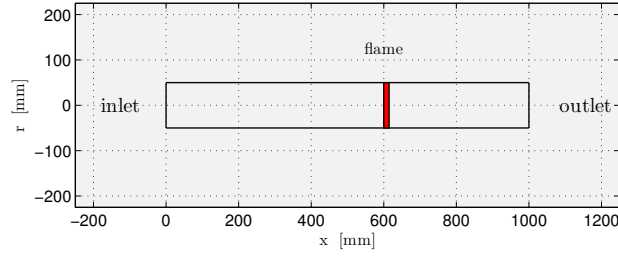

Figure 24: The Rijke of the example cases.

6.3.1   Case 1: Combining a linear HR model with a linear flame model

A linear Helmholtz resonator is attached to the Rijke tube system upstream of the flame, as shown in Fig. 25. The parameters of the resonator are shown in Table 1. The resonant frequency is $\sim 190\ Hz$. The effect of adding the resonator is shown in Fig. 26 where the resonator is seen to split the first unstable mode (200 Hz, 45 $rad\ s^{-1}$) into two stable modes (165 Hz, -10 $rad\ s^{-1}$) and (223 Hz, -6 $rad\ s^{-1}$). The other modes which are far away from the resonant frequency are almost unaffected.

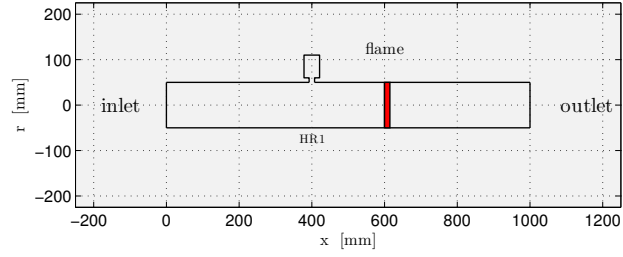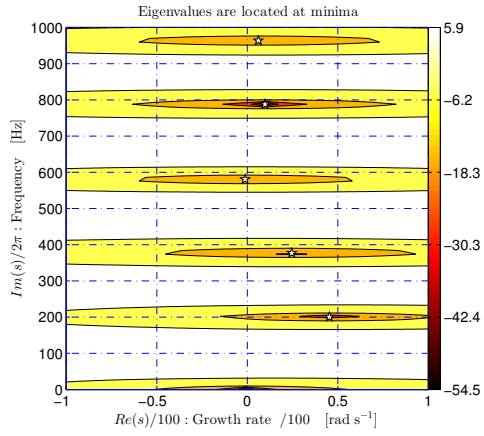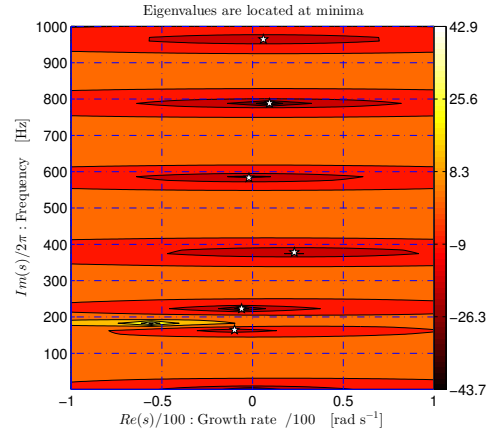| Location	Neck length	Neck area
400 mm	36.15 mm	235 mm^2
Neck Mach no.	Cavity volume	Cavity temperature
0.01	420000 mm^3	293.15 K

Table 1: *Linear HR configurations*

Figure 25: A Rijke tube with a HR attached upstream of the flame.

(a) Rijke tube with no dampers

(b) Rijke tube with one linear HR

Figure 26: Contour plot of eigenvalues with no dampers and with a linear HR.

6.3.2 Case 2: Combining a nonlinear HR model with a nonlinear flame model

The geometrical set-up of the case is the same as case 1. For the flame model, a saturation bound on the heat release rate is now employed. The mean flow Mach number in the resonator neck is assumed to be zero and a nonlinear discharge coefficient (set to 0.819) is used.
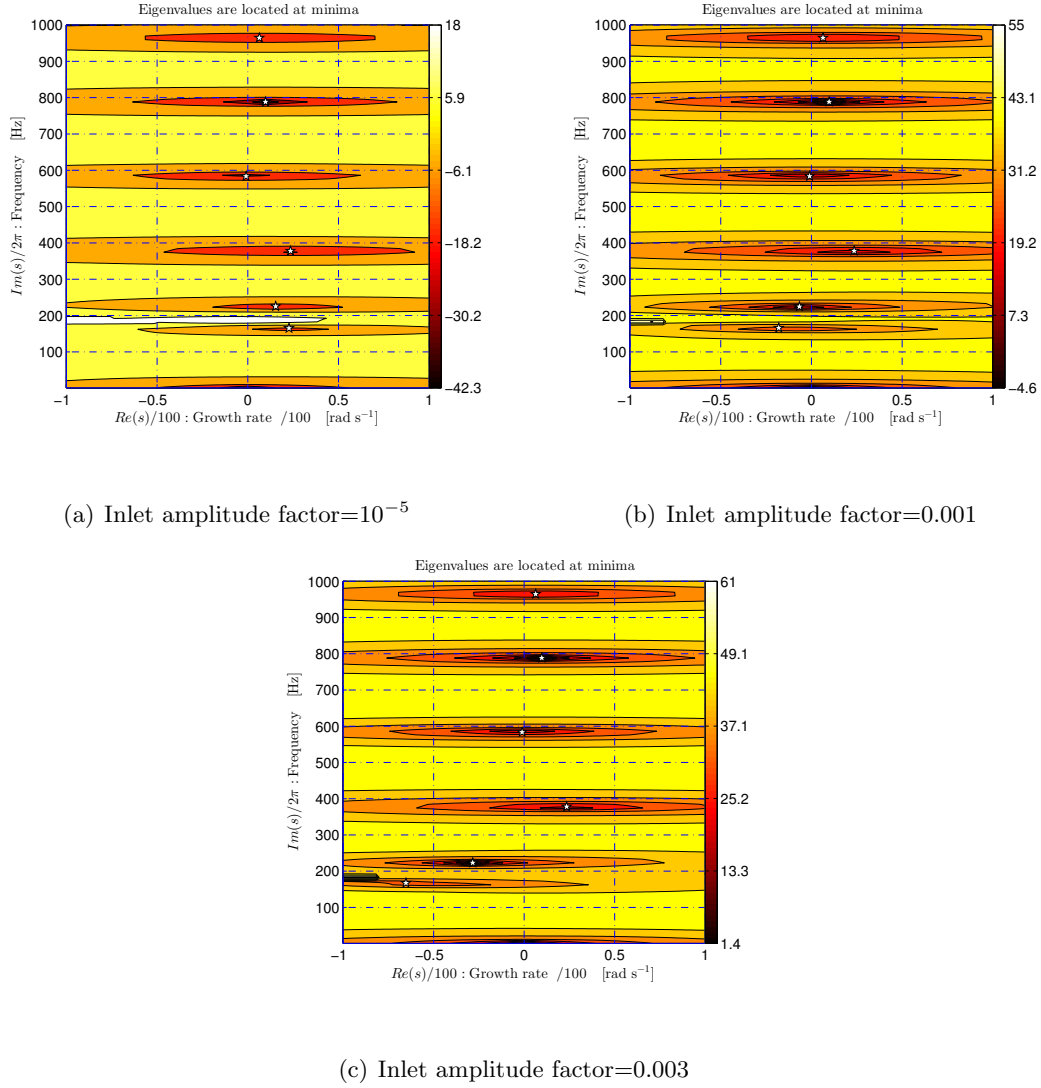

(a) Inlet amplitude factor=10^{-5}

(b) Inlet amplitude factor=0.001

(c) Inlet amplitude factor=0.003

Figure 27: Contour plot of the eigenvalues when combining a nonlinear HR and a nonlinear flame model.

56

Figure 27 shows the eigenvalues for three different inlet amplitude factors. It can be seen that the effect of the HR, as before, is to split the first original unstable mode (shown in Fig. 26(a)) into two modes (which may be stable or unstable). By increasing the inlet acoustic amplitude factor from 10^{-5} to 0.001, and then to 0.003, the two modes move from (165 Hz, 23 rad s^{-1}) and (225 Hz, 15 rad s^{-1}) to (166 Hz, -18 rad s^{-1}) and (224 Hz, -7 rad s^{-1}), and then to (167 Hz, -65 rad s^{-1}) and (223 Hz, -28 rad s^{-1}). The growth rate reduces with increased amplitude factor due to the increased damping performance of the HR. Modes which are further away see their growth rates reduces slightly, due to the nonlinear effects of the flame model.

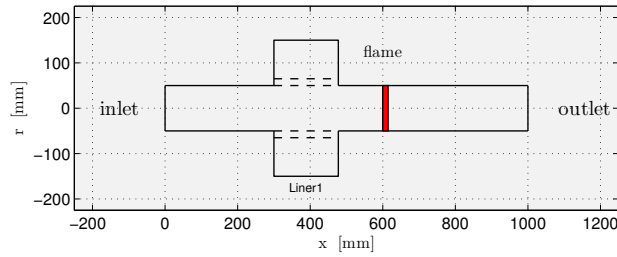### 6.3.3 Case 3: Combining a liner model with a linear flame model

Figure 28: A Rijke tube with a double liner.

A double liner is now attached to the Rijke tube, again upstream of the flame, as shown in Fig. 28. The liner parameters are shown in Table 2. The effect of the liner on the thermoacoustic modes is shown in Fig. 29. A significant reduction in the growth rates of all modes between 0 Hz and 1000 Hz is observed.

Type	Start location	Length	Temperature
Double + large cavity	300 mm	177.5 mm	293.15 K
First layer			
Hole radius	Hole distance	Hole mean Mach no.	Thickness
0.38 mm	3.3 mm	0.009	4.24 mm
Second layer			
Hole radius	Hole distance	Layer inner radius	Thickness
1.35 mm	17 mm	76 mm	3 mm

Table 2: Liner configurations
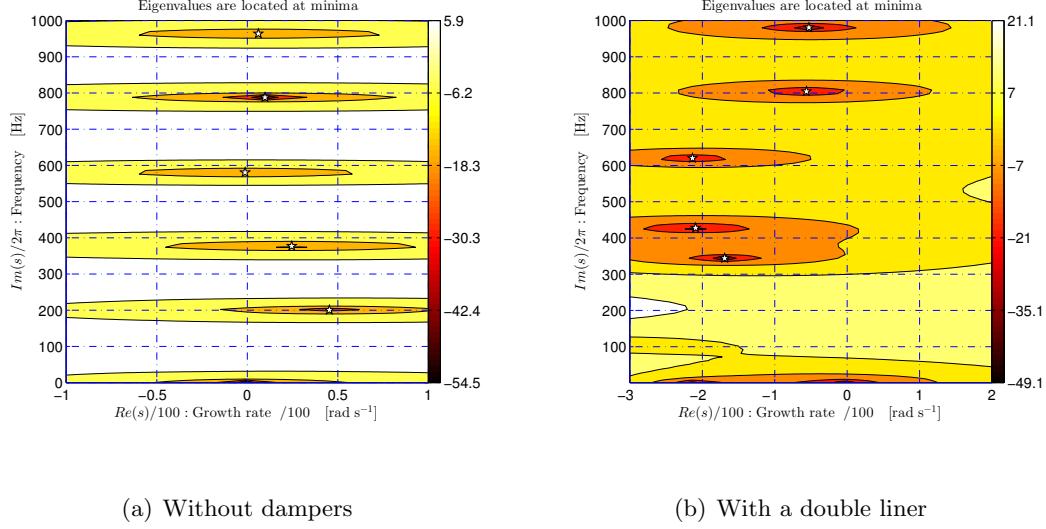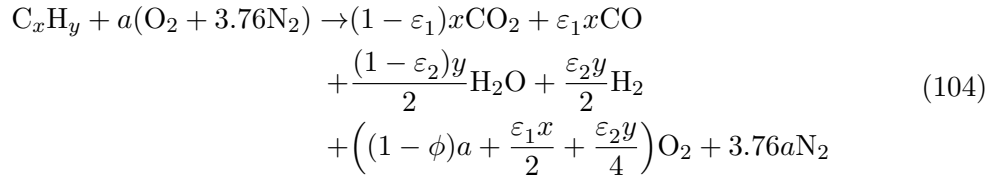
(a) Without dampers

(b) With a double liner

Figure 29: Contour plot of eigenvalues with no dampers and with a double perforated liner.

Appendix A: calculation of adiabatic temperature at dissociation equilibrium

A simple method is presented in this section to calculate the mass fractions of the species of hydro-carbon flame at dissociation equilibrium. To simplify the analysis, we only account for the major species and the products are assumed to be CO_2, CO, H_2O, H_2, O_2 and N_2 for hydrocarbon-air combustion. The species CO_2 and H_2O dissociate at high temperature, even for lean mixture conditions [85]. We assume an ε_1 amount of CO_2 and an ε_2 amount of H_2O dissociations, and the chemical reaction can be written as:

$$
\begin{aligned}
C_xH_y + a(O_2 + 3.76N_2) \rightarrow &(1 - \varepsilon_1)xCO_2 + \varepsilon_1 xCO \\
&+ \frac{(1 - \varepsilon_2)y}{2}H_2O + \frac{\varepsilon_2 y}{2}H_2 \\
&+ \left((1 - \phi)a + \frac{\varepsilon_1 x}{2} + \frac{\varepsilon_2 y}{4}\right)O_2 + 3.76aN_2
\end{aligned}
\tag{104}
$$

where $a = (x + y/4)\big/\phi$. The equilibrium constants for the dissociations of CO_2 and H_2O are:

$$K_{p,1} = \frac{(p_{\text{CO}}/p_0)(p_{\text{O}_2}/p_0)^{\frac{1}{2}}}{p_{\text{CO}_2}/p_0} = \frac{\varepsilon_1 b^{\frac{1}{2}}}{1-\varepsilon_1}\left(\frac{p}{p_0}\right)^{\frac{1}{2}} \tag{105}$$

$$K_{p,2} = \frac{(p_{\text{H}_2}/p_0)(p_{\text{O}_2}/p_0)^{\frac{1}{2}}}{p_{\text{H}_2\text{O}}/p_0} = \frac{\varepsilon_2 b^{\frac{1}{2}}}{1-\varepsilon_2}\left(\frac{p}{p_0}\right)^{\frac{1}{2}} \tag{106}$$

$$b = \frac{(1-\phi)a + \frac{\varepsilon_1 x}{2} + \frac{\varepsilon_2 y}{4}}{x + \frac{y}{2} + (4.76 - \phi)a + \frac{\varepsilon_1 x}{2} + \frac{\varepsilon_2 y}{4}} \tag{107}$$

Where p_0 denotes the standard-state pressure and p indicates local ambient pressure. For convenience, we set $p = p_0$. Using the trial-and-error method to determine the adiabatic temperature shown in [85](chapter 1, pages 68 - 90), one can obtain the mass fractions of the product constituents at equilibrium. Validation of this method is carried out by examining the evolution of adiabatic temperature T_f as a function the equivalence ratio ϕ, with the calculation results in [86], as shown in figure 30. A perfect match is seen, indicating that this method can be used to calculate the mass fractions of the species.
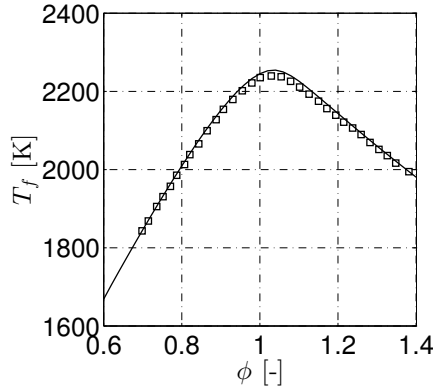

Figure 30: Evolutions of adiabatic temperature of methane-air flame as a function of the equivalence ratio ϕ. Markers: calculating results from [86]; solid line: current calculating results.

Acknowledgement

References

[1] J.R. Mahan and A. Karchemer. *Aeroacoustics of Flight Vehicles: Theory and Practice. Volume 1: Noise Sources*, volume 1, chapter Combustion and core noise, pages 483–517. WRDC Technical Report 90-3052, 1991.

[2] S. Candel. Combustion dynamics and control: Progress and challenges. *Proceedings of the Combustion Institute*, 29(1):1–28, 2002.

[3] S. Ducruix, T. Schuller, D. Durox, and S. Candel. Combustion dynamics and instabilities: Elementary coupling and driving mechanisms. *Journal of Propulsion and Power*, 19(5):722–734, 2003.

[4] S.M. Correa. Power generation and aeropropulsion gas turbines: From combustion science to combustion technology. *Proceedings of the Combustion Institute*, 27(2):1793–1807, 1998.

[5] T.C. Lieuwen and V. Yang, editors. *Combustion instabilities in gas turbines, Operational experience, Fundamental mechanisms, and Modeling*, volume 210 of *Progress in Astronautics and Aeronautics*. AIAA, Inc., 2005.

[6] A.P. Dowling and S.R. Stow. Acoustic Analysis of Gas Turbine Combustors. *Journal of Propulsion and Power*, 19(5):751–764, 2003.

[7] C.S. Goh and A.S. Morgans. The Influence of Entropy Waves on the Thermoacoustic Stability of a Model Combustor. *Combustion Science and Technology*, 185(2):249–268, 2013.

[8] A.A. Peracchio and W.M. Proscia. Nonlinear Heat-Release/Acoustic Model for Thermoacoustic Instability in Lean Premixed Combustors. *Journal of Engineering for Gas Turbines and Power*, 131(3):415–421, 1999.

[9] L. Crocco. Aspects of Combustion Stability in Liquid Propellant Rocket Motors Part I: Fundamentals. Low Frequency Instability With Monopropellants. *Journal of the American Rocket Society*, 21(6):163–178, 1951.

[10] M. Fleifil, A.M. Annaswamy, Z.A. Ghoneim, and A.F. Ghoniem. Response of a laminar premixed flame to flow oscillations: A kinematic model and thermoacoustic instability results. *Combustion and Flame*, 106(4):487–510, 1996.

[11] A.P. Dowling. Nonlinear self-excited oscillations of a ducted flame. *Journal of Fluid Mechanics*, 346:271–290, 1997.

[12] B.D. Bellows, Q. Zhang, Y. Neumeier, T. Lieuwen, and B.T. Zinn. Forced Response Studies of a Premixed Flame to Flow Disturbances in a Gas Turbine Combustor. In *41st AIAA Aerospace Sciences Meeting and Exhibit*, number AIAA-2003-824, Reno, Nevada, USA, 2003.

[13] R. Balachandran, B.O. Ayoola, C.F. Kaminski, A.P. Dowling, and E. Mastorakos. Experimental investigation of the nonlinear response of turbulent premixed flames to imposed inlet velocity oscillations. *Combustion and Flame*, 143(1-2):37–55, 2005.

[14] D. Durox, T. Schuller, N. Noiray, and S. Candel. Experimental analysis of nonlinear flame transfer functions for different flame geometries. *Proceedings of the Combustion Institute*, 32(1):1391–1398, 2009.

[15] N. Karimi, M.J. Brear, S.H. Jin, and J.P. Monty. Linear and non-linear forced response of a conical, ducted, laminar premixed flame. *Combustion and Flame*, 156(11):2201–2212, 2009.

[16] D. Durox, J.P. Moeck, J.F. Bourgouin, P. Morenton, M. Viallon, T. Schuller, and S. Candel. Flame dynamics of a variable swirl number system and instability control. *Combustion and Flame*, 160(9):1729–1742, 2013.

[17] Lord Rayleigh. *Theory of Sound (two volumes)*. Dover Publications, New York, 1877, re-issued 1945.

[18] A.P. Dowling and A.S. Morgans. Feedback control of combustion oscillations. *Annual Review of Fluid Mechanics*, 37:151–182, 2005.

[19] T. Poinsot, D. Veynante, F. Bourienne, S. Candel, E. Esposito, and J. Surget. Initiation and suppression of combustion instabilities by active control. *Proceedings of the Combustion Institute*, 22(1):1363–1370, 1989.

[20] N. Noiray, D. Durox, T. Schuller, and S. Candel. A unified framework for nonlinear combustion instability analysis based on the flame describing function. *Journal of Fluid Mechanics*, 615:139–167, 2008.

[21] S. Schimek, J.P. Moeck, and C.O. Paschereit. An Experimental Investigation of the Nonlinear Response of an Atmospheric Swirl-Stabilized Premixed Flame. *Journal of Engineering for Gas Turbines and Power*, 133(10):101502 (7 pages), 2011.

[22] F. Boudy, D. Durox, T. Schuller, G. Jomaas, and S. Candel. Describing Function Analysis of Limit Cycles in a Multiple Flame Combustor. *Journal of Engineering for Gas Turbines and Power*, 133(6):061502 (8 pages), 2011.

[23] F. A. Williams. Turbulent Combustion. In *The Mathematics of Combustion*, pages 97–131.

[24] A.P. Dowling. A kinematic model of a ducted flame. *Journal of Fluid Mechanics*, 394:51–72, 1999.

[25] J. Li and A.S. Morgans. Model based control of nonlinear combustion instabilities. In *the 21st International Congress on Sound and Vibration (ICSV21)*, Beijing, China, 2014.

[26] V. Bellucci, B. Schuermans, D. Nowak, P. Flohr, and C.O. Paschereit. Thermoacoustic Modeling of a Gas Turbine Combustor Equipped With Acoustic Dampers. *Journal of Turbomachinery*, 127(2):372–379, 2005.

[27] A.S. Morgans and S.R. Stow. Model-based control of combustion instabilities in annular combustors. *Combustion and Flame*, 150(4):380–399, 2007.

[28] Dong-Hyuk Shin and Timothy Lieuwen. Flame wrinkle destruction processes in harmonically forced, turbulent premixed flames. *Journal of Fluid Mechanics*, 721:484–513, March 2013.

[29] C-H. Wang and Ann P. Dowling. Actively tuned passive control of combustion instabilities. In *Advances in Combustion and Noise Control*, pages 45–64. Cranfield University Press, 2005.

[30] Preetham, Sai K. Thumuluru, H. Santosh, and Tim Lieuwen. Linear Response of Laminar Premixed Flames to Flow Oscillations: Unsteady Stretch Effects. *Journal of Propulsion and Power*, 26(3):524–532, May 2010.

[31] F.E. Marble and S.M. Candel. Acoustic disturbance from gas non-uniformities convected through a nozzle. *Journal of Sound and Vibration*, 55(2):225–243, 1977.

[32] A.S. Morgans and A.M. Annaswamy. Adaptive Control of Combustion Instabilities for Combustion Systems with Right-Half Plane Zeros. *Combustion Science and Technology*, 180(9):1549–1571, 2008.

[33] T. Sattelmayer. Influence of the Combustor Aerodynamics on Combustion Instabilities From Equivalence Ratio Fluctuations. *J. Eng. Gas Turbines Power*, 125(1):11–19, 2003.

[34] Aimee S. Morgans, Chee Su Goh, and Jeremy A. Dahan. The dissipation and shear dispersion of entropy waves in combustor thermoacoustics. *Journal of Fluid Mechanics*, 733(R2), 2013.

[35] S. Stow, A.P. Dowling, and T.P.Hynes. Reflection of circumferential modes in a choked nozzle. *Journal of Fluid Mechanics*, 467:215–239, 2002.

[36] P. Palies, D. Durox, T. Schuller, and S. Candel. Nonlinear combustion instability analysis based on the flame describing function applied to turbulent premixed swirling flames. *Combustion and Flame*, 158(10):1980–1991, 2011.

[37] Thierry Schuller, Daniel Durox, Paul Palies, and Sébastien Candel. Acoustic decoupling of longitudinal modes in generic combustion systems. *Combust. Flame*, 159(5):1921–1931, 2012.

[38] F.E.C. Culick. Nonlinear behavior of acoustic waves in combustion chambers–I. *Acta Astronautica*, 3(9-10):715–734, 1976.

[39] F.E.C. Culick. Nonlinear behavior of acoustic waves in combustion chambers–II. *Acta Astronautica*, 3(9-10):735–757, 1976.

[40] B.T. Zinn and M.E. Lores. Application of the Galerkin method in the solution of nonlinear axial combustion instability problems in liquid rockets. *Combustion Science and Technology*, 4:269–278, 1972.

[41] K. Balasubramanian and R. I. Sujith. Non-normality and nonlinearity in combustion–acoustic interaction in diffusion flames. *Journal of Fluid Mechanics*, 594:29–57, 2008.

[42] M.P. Juniper. Triggering in the horizontal Rijke tube: non-normality, transient growth and bypass transition. *Journal of Fluid Mechanics*, 667:272–308, 2011.

[43] P. Subramanian and R.I. Sujith. Non-normality and internal flame dynamics in premixed flame–acoustic interaction. *Journal of Fluid Mechanics*, 679:315–342, 2011.

[44] K. Kashinath, S. Hemchandra, and M.P. Juniper. Nonlinear thermoacoustics of ducted premixed flames: The influence of perturbation convection speed. *Combustion and Flame*, 160(12):2856–2865, 2013.

[45] D. Zhao. Transient growth of flow disturbances in triggering a Rijke tube combustion instability. *Combustion and Flame*, 159(6):2126–2137, 2012.

[46] Luca Magri and Matthew P. Juniper. Global modes, receptivity, and sensitivity analysis of diffusion flames coupled with duct acoustics. *Journal of Fluid Mechanics*, 752:237–265, 2014.

[47] B. Schuermans, V. Bellucci, and C.O. Paschereit. Thermoacoustic modelling and control of multi burner combustion systems. In *Proceedings of ASME Turbo Expo—Power for Land Sea and Air*, number GT2003-38688, Atlanta, Georgia, USA, 2003.

[48] S.R. Stow and A.P. Dowling. A Time-Domain Network Model for Nonlinear Thermoacoustic Oscillations. *Journal of Engineering for Gas Turbines and Power*, 131(3):031502 (10 pages), 2009.

[49] A.P. Dowling. The calculation of thermoacoustic oscillations. *Journal of Sound and Vibration*, 180(4):557–581, 1995.

[50] T. Poinsot and D. Veynante. *Theoretical and Numerical Combustion*. R.T. Edwards, Inc, 2005.

[51] Jingxuan Li and Aimee S. Morgans. Time domain simulations of nonlinear thermoacoustic behaviour in a simple combustor using a wave-based approach. *Journal of Sound and Vibration*, 2015.

[52] R.L. Raun, M.W. Beckstead, J.C. Finlinson, and K.P. Brooks. A review of Rijke tubes, Rijke burners and related devices. *Progress in Energy and Combustion Science*, 19(4):313–364, 1993.

[53] F. Boudy, D. Durox, T. Schuller, and S. Candel. Nonlinear mode triggering in a multiple flame combustor. *Proceedings of the Combustion Institute*, 33(1):1121–1128, 2011.

[54] A.S. Morgans and A.P. Dowling. Model-based control of combustion instabilities. *Journal of Sound and Vibration*, 299(1–2):261–282, 2007.

[55] Michael Feldman. Hilbert transform in vibration analysis. *Mechanical Systems and Signal Processing*, 25(3):735 – 802, 2011.

[56] N. Noiray, M. Bothien, and B. Schuermans. Investigation of azimuthal staging concepts in annular gas turbines. *Combustion Theory and Modelling*, 15(5):585–606, 2011.

[57] N. Noiray and B. Schuermans. On the dynamic nature of azimuthal thermoacoustic modes in annular gas turbine combustion chambers. *Proceedings of the Royal Society A*, 469(2151), 2013.

[58] Nicolas Tran. *Influence de la condition limite acoustique amont sur les instabilités de combustion de grande amplitude: conception dun système robuste de contrôle d'impédance*. PhD thesis, Ecolce Centrale Paris, 2009.

[59] Jingxuan Li. *Development of novel diagnostic techniques to measure heat release rate perturbations in flames*. PhD thesis, Ecole Centrale Paris, 2012.

[60] Jr. Marple, S.L. Computing the discrete-time ldquo;analytic rdquo; signal via fft. *Signal Processing, IEEE Transactions on*, 47(9):2600–2603, Sep 1999.

[61] T. Schuller, D. Durox, and S. Candel. Self-induced combustion oscillations of laminar premixed flames stabilized on annular burners. *Combustion and Flame*, 135(4):525–537, 2003.

[62] Ann P Dowling and J E Ffowcs Williams. *Sound and sources of sound*. John Wiley & Sons, Inc. New York, USA, 1983.

[63] A Cummings. Acoustic nonlinearities and power losses at orifices. *AIAA journal*, 22(6):786–792, 1984.

[64] Iain DJ Dupère and Ann P Dowling. The absorption of sound by helmholtz resonators with and without flow. *AIAA 2002*, 2590, 2002.

[65] V Bellucci, P Flohr, CO Paschereit, and F Magni. On the use of helmholtz resonators for damping acoustic pulsations in industrial gas turbines. *Journal of engineering for gas turbines and power*, 126(2):271–275, 2004.

[66] Iain DJ Dupère and Ann P Dowling. The use of helmholtz resonators in a practical combustor. *Journal of engineering for gas turbines and power*, 127(2):268–275, 2005.

[67] Dan Zhao, Chris A'Barrow, Aimee S Morgans, and Jon Carrotte. Acoustic damping of a helmholtz resonator with an oscillating volume. *AIAA journal*, 47(7):1672–1679, 2009.

[68] MS Howe. On the theory of unsteady high reynolds number flow through a circular aperture. *Proceedings of the Royal Society of London. A. Mathematical and Physical Sciences*, 366(1725):205–223, 1979.

[69] IJ Hughes and AP Dowling. The absorption of sound by perforated linings. *Journal of Fluid Mechanics*, 218:299–335, 1990.

[70] Jeff D Eldredge and Ann P Dowling. The absorption of axial acoustic waves by a perforated liner with bias flow. *Journal of Fluid Mechanics*, 485:307–335, 2003.

[71] Xiaodong Jing and Xiaofeng Sun. Experimental investigations of perforated liners with bias flow. *The Journal of the Acoustical Society of America*, 106(5):2436–2441, 1999.

[72] Jochen Rupp, Jon Carrotte, and Adrian Spencer. Interaction between the acoustic pressure fluctuations and the unsteady flow field through circular holes. *Journal of Engineering for Gas Turbines and Power*, 132(6):061501, 2010.

[73] A Scarpato, N Tran, S Ducruix, and T Schuller. Modeling the damping properties of perforated screens traversed by a bias flow and backed by a cavity at low strouhal number. *Journal of Sound and Vibration*, 331(2):276–290, 2012.

[74] MS Howe, MI Scott, and SR Sipcic. The influence of tangential mean flow on the rayleigh conductivity of an aperture. *Proceedings of the Royal Society of London. Series A: Mathematical, Physical and Engineering Sciences*, 452(1953):2303–2317, 1996.

[75] X Sun, X Jing, H Zhang, and Y Shi. Effect of grazing–bias flow interaction on acoustic impedance of perforated plates. *Journal of Sound and Vibration*, 254(3):557–573, 2002.

[76] Bernhard Ćosić, Thoralf G Reichel, and Christian Oliver Paschereit. Acoustic response of a helmholtz resonator exposed to hot-gas penetration and high amplitude oscillations. *Journal of Engineering for Gas Turbines and Power*, 134(10):101503, 2012.

[77] B Ćosić, D Wassmer, S Terhaar, and CO Paschereit. Acoustic response of helmholtz dampers in the presence of hot grazing flow. *Journal of Sound and Vibration*, 2014.

[78] Michael S Howe. *Acoustics of fluid-structure interactions*. Cambridge University Press, 1998.

[79] PD Dean and BJ Tester. Duct wall impedance control as an advanced concept for acoustic suppression nasa contractor rept. *CR-134998, Nov*, 1975.

[80] Valter Bellucci, Christian Oliver Paschereit, and Peter Flohr. Impedance of perforated screens with bias flow. *AIAA Paper*, 2437:17–19, 2002.

[81] Jochen Rupp, Jon Carrotte, and Michael Macquisten. The use of perforated damping liners in aero gas turbine combustion systems. *Journal of Engineering for Gas Turbines and Power*, 134(7):071502, 2012.

[82] William H Press. *Numerical recipes 3rd edition: The art of scientific computing*. Cambridge university press, 2007.

[83] Simon R Stow and Ann P Dowling. Modelling of circumferential modal coupling due to helmholtz resonators. In *ASME Turbo Expo 2003, collocated with the 2003 International Joint Power Generation Conference*, pages 129–137. American Society of Mechanical Engineers, 2003.

[84] Simon R Stow and Ann P Dowling. A time-domain network model for nonlinear thermoacoustic oscillations. *Journal of engineering for gas turbines and power*, 131(3):031502, 2009.

[85] Kenneth Kuan-yun Kuo. *Principles of Combustion*. Wiley-Interscience, New Jersey, 2005.

[86] C.K. Law, A. Makino, and T.F. Lu. On the off-stoichiometric peaking of adiabatic flame temperature. *Combust. Flame*, 145(4):808–819, 2006.